Multimode Electron Tomography sheds light on synthesis, structure, and properties of complex metal-based nanoparticles

Kellie Jenkinson, Luis M. Liz-Marzán* and Sara Bals*

Dr. Kellie Jenkinson and Prof. Sara Bals
Address: EMAT and NANOlab Center of Excellence, University of Antwerp, 2020 Antwerp, Belgium
E-mail: sara.bals@uantwerpen.be

Prof. Luis M. Liz-Marzán
Address:
1) CIC biomaGUNE, Basque Research and Technology Alliance (BRTA), 20014 Donostia-San Sebastián, Spain
2) Centro de Investigación Biomédica en Red de Bioingeniería Biomateriales, y Nanomedicina (CIBER-BBN), 20014 Donostia-San Sebastián, Spain
3) Ikerbasque, Basque Foundation for Science, 48009 Bilbao, Spain
E-mail: llizmarzan@cicbiomagune.es

Electron tomography has become a cornerstone technique for the visualization of nanoparticle morphology in three dimensions. However, to obtain in-depth information about a nanoparticle beyond surface faceting and morphology, different electron microscopy signals must be combined. The most notable examples of these combined signals include annular dark-field scanning transmission electron microscopy (ADF-STEM) with different collection angles and the combination of ADF-STEM with energy dispersive X-ray or electron energy loss spectroscopies. This review summarizes the experimental and computational development of various multimode tomography techniques in connection to fundamental materials science challenges that multimode tomography has been instrumental to overcoming. Although the techniques can be applied to a wide variety of compositions, we restrict ourselves to metal and metal oxide nanoparticles for the sake of simplicity. Current challenges and future directions of multimode tomography are additionally discussed.

1. Introduction

Nanoparticles (NPs) have revolutionized the fields of catalysis, diagnostic and therapeutic medicine, battery technology and memory storage devices, therefore providing solutions to a wide range of social and economic challenges.[1–3] Increasingly complex materials can be prepared for optimized application performance from a wealth of synthetic techniques, including surfactant-, seed-, and additive-mediated procedures,[4–8] which has directly challenged materials characterization to bridge the knowledge gap between synthesis and application performance. [3,9–11] The crystallinity, surface faceting, morphology, as well as elemental distribution and oxidation state, have a profound influence upon nanomaterials properties; all of which can be understood by means of transmission electron microscopy (TEM).

Electron tomography (ET) has become an indispensable technique for the three-dimensional (3D) characterization of nanoparticles during the last decade. [12–19] Traditionally, ET has primarily been used to understand surface faceting or to accurately quantify anisotropic morphologies for nanomaterials that cannot be properly understood when using two-dimensional (2D) imaging only. In fact, even seemingly simple and spherical morphologies cannot always be correctly interpreted from a 2D projection, as even slightly asymmetric morphologies may have a preferential orientation on a TEM grid.[20] ET overcomes these challenges by acquiring 2D projection images of the same NP every few degrees (typically 1° - 3°) over a tilt range of -80º to +80°. The recorded 2D projections are then aligned using a cross-correlation-based approach and reconstructed using dedicated algorithms such as weighted back-projection (WBP),[21] simultaneously iterative reconstruction technique (SIRT),[22] expectation maximization (EM),[23] total variation minimization (TVM) [24] or the discrete algebraic reconstruction technique (DART).[25,26] A significant limitation of

conventional ET is related to the time required for acquisition of a full tilt series (~40 minutes to several hours, depending on the angular increment needed). Significant progress has been made by several groups, resulting in the acquisition of a complete tomogram within few minutes or even less than a minute.[27, 28] The implementation of fast electron tomography is particularly beneficial for *in situ* experiments, in addition to the study of beam sensitive samples that might not withstand the long beam exposures required for conventional tomography experiments.[29–31] Interested readers are directed to a recent review by Albrecht *et al.*[32] Although the ideal angular range to image a NP in 3D would be 180°, within an electron microscope there is limited space above and below the sample due to upper and lower objective pole pieces that restrict rotation. Such a restricted rotation represents another significant challenge in ET: the so-called "missing wedge". Missing wedge artifacts result in blurring, stretching and distortions within the reconstructed image, at those regions where 2D projections could not be acquired, resulting in reduced resolution and loss of information. There are several practical techniques applied to the mitigation or minimization of missing wedge artifacts for conventional ET, including double-tilt ET which can be applied to small NPs as a second tilt series is acquired after grid rotation by 90 °.[33,34,35] Double-tilt ET therefore minimizes the missing wedge artifacts from a 'wedge' to a 'pyramid' of missing information, however aligning the two independent tilt series can be challenging and the extra electron dose and acquisition time are inevitably doubled compared to conventional ET, therefore restricting applicability to the more stable samples. Alternatively, on-axis ET or ET using a rotation holder have been developed to entirely remove missing wedge artifact contributions. The former requires the sample to be fashioned into a thin needle by FIB milling to enable unrestricted sample rotation and the acquisition of a full tilt series (± 180 °), which is inappropriate for small freestanding NPs.[36,37] In contrast, the latter uses a precisely prepared rotation holder stub by FIB milling. If a NP can be deposited at the very tip of the rotation stub, it is possible to image a freestanding NP with unhindered 360 ° rotation and eliminate missing wedge artifacts.[38] In addition to the physical measures for

missing wedge artifact minimization, advanced computational reconstruction techniques and the incorporation of neural networks are also a thriving area of research.[26,39,40]

Thanks to the progress in instrument and software development, ET has become a crucial tool to determine 3D morphology and to obtain surface faceting information, while atomic-resolution tomography can additionally yield detailed information on crystallinity, provided the samples are sufficiently thin. On the other hand, there is still a wealth of information that cannot be accounted for by using traditional ET experiments alone, such as elemental and oxidation state distributions, which play a significant role in determining the physicochemical properties of the NPs. Multimode tomography (MMT), as the name itself implies, uses at least two different TEM techniques - or 'modes' - to obtain projections of a specimen in 2D, which can be subsequently reconstructed to achieve a 3D multimode tomogram. The broad term 'mode' can involve different imaging or acquisition techniques and even combine imaging with spectroscopy or diffraction, so that a variety of possible measurement combinations can satisfy the 'multimode' label. Unfortunately, not every signal that can be measured within an electron microscope can be used for ET. Indeed, the collected signals must satisfy the projection requirement, meaning that the intensity of acquired images must be a monotonic function of a certain property of the sample under investigation.[41] For example, bright field TEM (BF TEM) images acquired for crystalline NP are partly based on diffraction contrast, which is sensitive to the orientation of the particle relative to the incident electron beam. Consequently, the projection requirement is not fulfilled in this case.

Throughout this review, we discuss measurement combinations designed to target structural, compositional, and valency information within nanostructures comprising metals or metal oxides. Moreover, we highlight acquisition and processing considerations for each technique. Finally, we express our view of the future of MMT and key challenges that must be overcome.

2. Results and Discussion

2.1 Multimode tomography by ADF-STEM

Conventional ET experiments in materials science are mostly achieved by acquiring high angular annular dark field scanning transmission electron microscopy (HAADF STEM) images at discrete angles. The predominance of HAADF STEM for ET in materials science is owed to its signal intensity, which is proportional to the atomic number squared (Z^2) of the elements in the sample, as well as to its projection thickness. As such, the technique obeys the projection requirement for tomography. However, there are important cases where HAADF STEM images can disobey the projection requirement, the most prominent of which is observed for large NPs where the thicker regions of the sample can dampen the intensity of the HAADF signal in a non-linear fashion.[42] The non-linear damping results in an observed 'cupping artifact' which is displayed as a loss of intensity towards the center or thicker region of the NP due to excessive damping.[43] In the most severe cases, cupping artifacts can even make NPs artificially appear hollow, thereby risking a mischaracterization of the material.[44] One suggested solution to overcome the cupping artifact includes the use of calibrated detectors and a linear transformation of the HAADF STEM intensities to express these as a fraction of the incoming beam intensity.[42] More recently, cupping artifacts for large assemblies of NPs were overcome by turning the grid upside down and re-acquiring the same tilt series on the reverse-side of the same assembly, thus capturing missing information lost through damping.[45] Alternative causes for HAADF STEM images to break the projection requirement include electron tunneling through atomic columns giving higher signal intensities for NPs perfectly in zone, although this is mostly applicable to atomic resolution ET which is beyond the scope of this review. For lower angle STEM imaging, such as so-called 'medium' or 'low' angle annular dark field imaging (MAADF or LAADF respectively), the collection angle of the annular detector is adjusted to collect both coherent and incoherent scattered electrons. In this manner, diffraction contrast will contribute to image formation, so that information regarding the presence of

defects can be extracted, but at the same time MAADF and LAADF imaging modes violate the projection requirement for ET. As discussed in sections 2.1.1 and 2.1.2, such signals must therefore be combined with HAADF imaging to obtain accurate 3D reconstructions.[46] As such, the combinations of MAADF or LAADF with HAADF imaging earn the label of 'multimodal'. In general, the collection angles can be fine-tuned for a given experiment through changes in camera length. In some cases, HAADF, MAADF and LAADF signals can even be collected simultaneously, depending on the specific TEM instrument being used.

### 2.1.1 MMT for visualization of lattice defects

The introduction of twinning planes or structural defects within metal nanoparticles can have a profound influence upon e.g. their plasmonic or catalytic behavior. In particular, catalytic activity is closely connected to the crystallographic nature of surface facets and crystallographic defects on which chemical reactions take place.[47–52] Several techniques can be used to image twinning planes and other defects in 3D using ET. Perhaps the most obvious option is using atomic-resolution HAADF STEM tomography, where an atomic-resolution HAADF STEM tilt series can be reconstructed in 3D.[25, 53] However, significant restrictions apply to atomic-resolution ET that must be taken into consideration, such as access to an aberration-corrected microscope capable of atomic resolution STEM imaging. Moreover, atomic-resolution ET requires high magnification, which severely restricts the size of the particle under investigation or limits acquisition to a smaller region within a larger particle. Finally, the time taken at each angle to reduce remaining aberrations, to bring the area of interest into the field of view and to adjust defocus takes considerably longer than in conventional tomography and is difficult to automate. This procedure therefore requires an increased electron dose to collect all images in a tilt series and consequently increases the risk of damaging the structure under investigation.

At the nanometer scale, several electron microscopy methods have been developed to visualize crystalline defects in 3D, such as weak beam electron tomography[54] or scanning electron diffraction.[55] Alternatively, imaging-based MMT can be used in most modern mid-resolution microscopes, to combine HAADF STEM with MAADF STEM or LAADF STEM signals.[56,57] Image-based MMT experiments can be acquired at much lower magnification than their atomic resolution counterparts and therefore an entire nanoparticle can usually be imaged. Furthermore, HAADF, MAADF and LAADF signals can often be collected simultaneously, thereby reducing sample exposure to the electron beam.

In a representative piece of work, Winckelmans *et al*. imaged twin boundaries within pentatwinned Au nanoparticles with decahedral morphology, by combining HAADF and LAADF signals during a single ET experiment.[46] The study showed that increasingly more diffraction information was included as the inner collection angle of the detector was lowered from HAADF > MAADF > LAADF and that the visualization of twinning planes, based on such a diffraction contrast, increased as shown in **Figure 1**a-c. However, the final reconstructed 3D structure displayed greater errors when quantifying morphology, compared to a standard HAADF reconstruction. To perform a quantitative comparison, the "shape error" [39] was used, which is defined by the number of voxels within the MAADF or LAADF reconstruction that are labelled differently compared to the idealized HAADF tomography equivalent. This shape error within the 3D reconstruction was shown to increase for MAADF (4.4%) and LAADF (8.0%), due to successive projection requirement violations. By combining morphology information from a nearly diffraction-free HAADF STEM reconstruction and lattice plane information from the LAADF reconstruction, an overall compromise could be achieved to accurately visualize morphology and twinning within the same NP (Figure 1d-f).[46] The HAADF-LAADF multimode approach was also used to identify the mechanistic influence of seed nanoparticles during the seed-mediated synthesis. Au@Pd pentatwinned decahedra were

used in this case as the seeds from which Au pentatwinned bipyramids would grow. The location of the seed nanoparticle and twinning planes could be investigated in 3D because of the lower atomic number Z for Pd compared to Au, as shown in Figure 1g. The study showed that the bimetallic seed always resided at the center of the transversal direction (at the connection point of the five twins). Unexpectedly, the location of the seed in the longitudinal direction appeared more off-center when a higher Pd coverage was present on the decahedral Au seed. A summary of the seed-mediated mechanistic study is presented in Figure 1g-i. The outcome of this study illustrates that size, composition, and crystallinity of the seeds are critical parameters to ensure homogeneous symmetry breaking and high-quality anisotropic NPs, while identifying seed displacement as a further parameter to be considered when designing future synthetic routes.
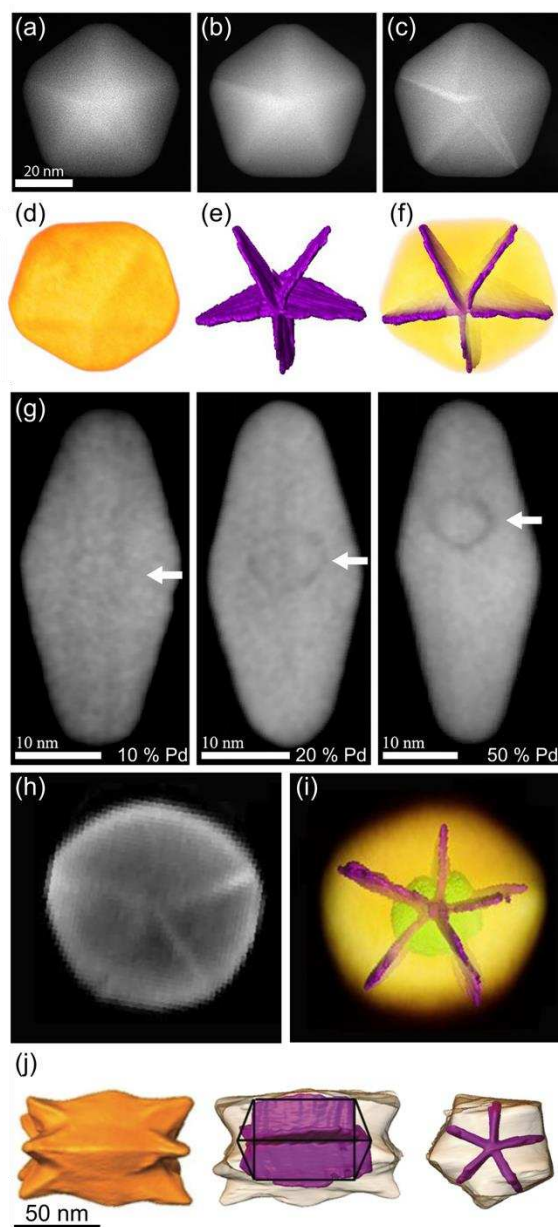
Figure 1. (a-c) STEM projections of an Au decahedral particle showing increasing twin boundary diffraction contrast when transitioning from HAADF (a) to MAADF (b) and LAADF (c) acquisition modes. (d-f) HAADF-LAADF MMT reconstruction of an Au decahedral NP showing the accurately determined shape extracted from HAADF STEM tomography (d), segmentations of twin boundaries visualized by LAADF STEM tomography (e), and an overlay of morphology and twin boundaries in 3D (f). (g) Orthoslices through the 3D HAADF STEM reconstructions of bipyramids prepared by growth on Au@Pd seed particles containing increasing amounts of Pd (10, 20 and 50 mol%). The seed particle becomes easier to visualize and shows a greater deviation from the NPs longitudinal center with increasing Pd concentration. Seed particle location is identified by white arrows. (h) Transversal orthoslice thorough the bipyramid NP's LAADF STEM reconstruction to show twin boundaries. (i) Segmented seed particle (green, 20% Pd) and twin boundaries (purple) superimposed on a HAADF STEM tomography reconstruction of an Au bipyramid NP, visualized along the long axis. (j) HAADF - LAADF MMT of branched pentatwinned Au nanorods showing conventional HAAD reconstruction (orange) and twinning planes (purple) identified by LAADF tomography.[58] Reprinted with permission.[46, 58]

9

In a related study, 3D HAADF-LAADF imaging was used by Smith *et al.* to investigate growth mechanisms of faceted and branched pentatwinned AuPd rods shown in Figure 1j.[58] Direct visualization of the seed particle within the larger structure enabled key mechanistic insight into seed-mediated growth strategies; showing that kinetic growth of nanoparticles was dominant at seed facets rather than seed vertices, as had previously been proposed for this system. This study could also track the formation of the overall branched structures to demonstrate the high relevance of NP seed features to induce specific faceting, branching, and twinning within the final NP. Studies such as this one provide key understanding regarding the role that twinning planes play within the seed particle and offer a unique perspective on the future design of complex branched NPs from fcc metals.[58]

2.1.2 MMT for hard-soft nanocomposites

Core@shell hybrid nanomaterials have grown in popularity due to their diverse and easily tailored properties for catalysis, optics and biosensing applications, among others.[3, 59, 60] As an example, the combination of inorganic metal cores such as plasmonic Au or magnetic Fe_2O_3 NPs coated with porous and biocompatible surfaces such as silica or metal-organic framework (MOF) structures have been used for controlled photothermal or magnetic-hyperthermal drug delivery devices.[61–63] The emerging field of complex hard-soft composite nanomaterials such as 'high atomic number' metal nanoparticles encapsulated within 'low atomic number' silica or MOF shells, represents a considerable challenge for reliable TEM characterization. As the intensity of HAADF signals is strongly dependent upon atomic number (Z^2), a large difference in Z results in an enhanced difference in the collected signal intensity. Such a large signal range is not always possible to measure simultaneously within the dynamic range of HAADF detectors and is further complicated when trying to mitigate diffraction contrast. Although it is

always possible to tune the detector for a dedicated intensity range, imaging low-Z elements will often lead to saturated areas from high-Z regions. Furthermore, collecting high- and low-intensity ranges consecutively is extremely time- and dose-inefficient, which must be considered when investigating beam-sensitive materials [60, 64, 65]

Sentosun *et al.* have nicely illustrated the use of MMT to image hybrid nanocomposites, by combining HAADF-LAADF imaging for the characterization of gold NPs coated with mesoporous silica shells (Au@SiO$_2$).[66] This study enabled the simultaneous imaging of structural details for the core and the shell. In particular, the mesoporous network in the SiO$_2$ shell could be resolved with high fidelity, which is of fundamental importance toward designing such nanocomposite NPs for applications in drug delivery, sensing or catalysis. The result of a LAADF acquisition and conventional reconstruction of such projections is shown in Figure 2a-c. The reconstruction shows severe artifacts, such as a large dark region surrounding the core (shown by white arrows in Figure 2b), as well as streaking within the reconstruction, which result in loss of information and a risk of misinterpretation. Streaking artifacts and missing information within the reconstruction are introduced because of diffraction contrast and high intensity contrast between the core and the shell materials during acquisition.[67] To minimize such artifacts, Sentosun proposed removing the problematic Au signal from each LAADF projection prior to the reconstruction, as illustrated in Figure 2e-h. Pixels originating from the Au core are removed by thresholding (Figure 2e), followed by inpainting (Figure 2f) based on the iterative propagation of surrounding texture. Next, the inpainted LAADF projections are reconstructed to yield the 3D structure of the SiO$_2$ shell, showing a network of radial pores and a substantial reduction in the aforementioned artifacts (Figure 2g). Finally, the LAADF reconstruction was combined with a HAADF tomography reconstruction showing the Au nanorod only, so as to achieve an overall hard-soft composite structure in unprecedented detail (Figure 2h). It is important to note that extraction of the Au LAADF signal was only possible

because the morphology and position of the Au core was accurately mapped through the simultaneous collection of a HAADF tomogram, which could be combined with the LAADF tomogram post-reconstruction.
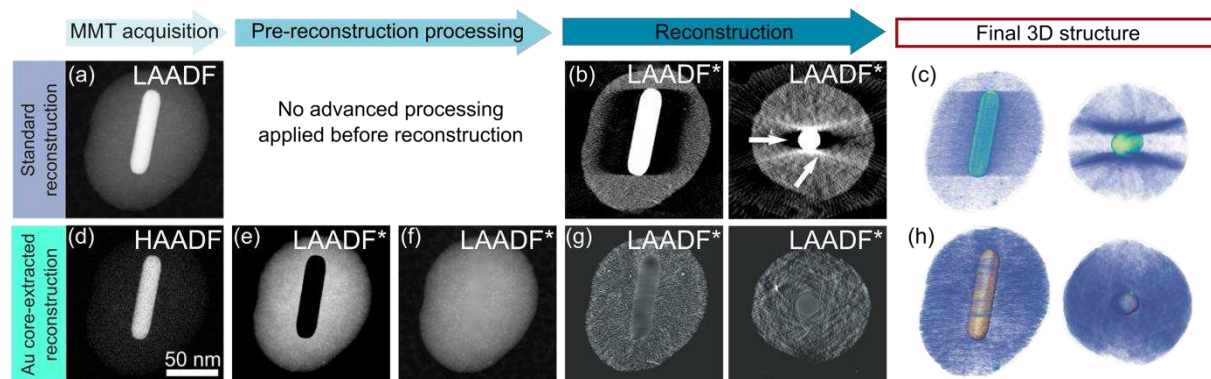
Figure 2. (a-c) Processing workflow and outcome for a conventional LAADF reconstruction procedure, compared to a novel inpainting technique (e-h) where the LAADF* label is used to indicate a modified LAADF projection. (a) and (d) show LAADF and HAADF projections, respectively, for an Au@SiO$_2$ NP. Shown in (b) are orthoslices extracted from a conventionally reconstructed LAADF tilt series, white arrows show intense reconstruction artifacts. The volume rendering of the LAADF STEM tomogram in (c) shows the Au core (green) and lower-intensity SiO$_2$ shell (blue). The image in (e) shows the product of Au core extraction followed by inpainting of empty pixels from the original LAADF dataset (f). Orthoslices extracted from the inpainted LAADF reconstruction (g) show the lack of the bright Au core and a significant reduction of artifacts compared to (b). Combined HAADF STEM and LAADF STEM reconstructions (h) show the Au core (yellow) and SiO$_2$ shell (blue) with high signal intensities and minimum reconstruction artifacts. Adapted with permission.[66]

In a related study, HAADF-LAADF MMT was applied to visualize the 3D structure of composite nanoparticles in which an Au spherical core was overgrown through radial mesopores within a SiO$_2$ shell, resulting in branched-Au@SiO$_2$ nanocomposites. Understanding the efficiency of the encapsulated Au tips for surface-enhanced Raman scattering (SERS) detection of molecules diffusing from solution through the pore openings, required accurate 3D characterization of the morphologies of both the Au core and the SiO$_2$ shell.[68] This technique was subsequently extended to investigate metal nanoparticles with various shapes, encapsulated within low atomic number ZIF-8 MOF shells, in the context of

understanding analyte diffusion which was highly dependent on the 3D structure of the nanocomposite.[69, 70]

2.2 EDXS Tomography

The preparation of multimetallic NPs with well-defined size, morphology, composition, and elemental distribution has been the central focus of materials science for decades.[10, 71, 72] This intense research interest is owed to their superior properties, often observed specifically for anisotropic structures.[1, 6, 10, 62–65] Again, NP characterization to understand structure-activity relationships within these complex systems is a significant challenge.

As mentioned in section 2.1, the signal intensity in HAADF STEM is sensitive to both projection thickness and atomic number. It is therefore possible to infer elemental distribution information from HAADF signal intensities, but this is however only feasible for relatively simple cases, featuring a sufficiently large difference between the atomic number of the different elements.[31,77] Elemental distribution mapping in 2D is usually carried out by energy dispersive X-ray spectroscopy (EDXS), in which X-rays with element-specific energy are emitted from an irradiated sample during an ionization event. As the total intensity of emitted X-rays is proportional to the number of atoms interacting with the electron beam, EDXS analysis enables elemental quantification.[78] However, compared to HAADF STEM imaging, EDXS mapping is hindered by a poor signal-to-noise ratio (SNR) due to the small detector size and low probability of X-ray generation fluorescence yield, which is intrinsic to an element and increasingly problematic when reducing Z.[79] Due to the low SNR of EDXS, elemental mapping is often time consuming and requires high electron beam doses, which in turn are problematic for beam-sensitive materials.

2.2.1 Considerations for EDXS tomography

In a similar manner to HAADF STEM imaging, X-ray signals collected from EDXS are incoherently scattered and, therefore, they can in principle be used as an input for reconstruction, as they do satisfy the projection requirement. However, several factors must be considered when transitioning from 2D to 3D elemental mapping by EDXS. A first limitation is the significant increase in the electron dose required for each projection in an EDXS tomography tilt series. Consequently, the number of projection images in the tilt series is reduced to e.g. 15 EDXS 2D maps (assuming 10° increments). To enable an accurate alignment of these images, and to improve the spatial resolution of the final 3D reconstruction, an independent HAADF STEM tilt series of the same object of interest is collected. All of this again represents a severe problem for beam-sensitive materials (e.g. MOFs), but even metal or metal oxide nanoparticles might undergo reshaping upon prolonged beam exposure. Additionally, the distribution of elements within an alloy may also potentially change during acquisition, which is especially problematic as the measurement of elemental distribution is often the primary aim of EDXS tomography. Moreover, early attempts to perform 3D EDXS experiments were complicated by the specimen-detector geometry, whereby a significant fraction of the generated X-rays was blocked by the sample holder and therefore not measured by the EDXS detector.[80] As a result, so-called "shadowing effects" were observed.

The implementation of modern integrated detectors such as the Super-X or Ultra-X detectors[81] (which both combine several EDXS detectors placed symmetrically above the sample location) made high-quality EDXS tomography possible.[82] Modern EDXS detectors allow for acceptable acquisition times (5-10 minutes/map) and, most importantly, overcome the most severe shadowing effects.[83] However, even with modern multiple-detector EDXS systems, shadowing is problematic when aiming at quantitative 3D EDXS reconstructions, as the extent

of detector shadowing varies at different angles. Therefore, such tilt series do not obey the projection requirement necessary to reconstruct a 3D structure without post-acquisition correction. Several techniques have been proposed to overcome this limitation, such as: (1) the combination of individual detector signals;[84, 85] (2) varying EDXS map acquisition time at each angle, guided by external holder calibrations;[80] and (3) signal intensity normalization at each angle.[79, 86] An alternative approach will be discussed in Section 2.2.4.

2.2.2 EDXS tomography for the investigation of complex 3D structures

The principal objective of EDXS tomography experiments is to identify composition and elemental distributions within complex nanoarchitectures, so that their morphology and composition can be correlated with their physicochemical properties. Importantly, such complex structures make elemental mapping in 2D insufficient to understand the characteristics that are crucial to inform and direct next-stage materials design.

An excellent example of materials displaying unique morphologies and multiple interfaces within the same particle, is provided by so-called Janus or patchy NPs, which are of great interest due to the possibility of functionalizing different patches independently, e.g. for biomedical applications or oil-water emulsion stabilization.[6, 87–91] The elemental distribution of Fe_3O_4-Au Janus plasmonic-magnetic anisotropic NPs has been investigated by EDXS tomography by Reguera *et al*.[92] Due to the unique star-sphere morphology of the plasmonic part, information on the elemental distribution could not be reliably extracted from HAADF STEM images, as intensity variations could arise not only from atomic number differences but also from mass thickness contrast. Additionally, the complex Janus architecture was difficult to assess through HAADF STEM tomography alone because the lighter iron oxide phase did not provide sufficient contrast, as compared to Au. Therefore, a combined HAADF STEM and

EDXS tomography experiment was used to identify the 3D elemental distribution of Au and Fe within the structure, as shown in **Figure 3**a. These investigations confirmed that Au did not fully encapsulate the Fe-based lobe, but two lobes with independently accessible surfaces were available for further functionalization.

In a similar manner, EDXS tomography was used to characterize the morphology and elemental distribution within complex bimetallic CoFe dumbbell structures by Liakakos *et al.*, as shown in Figure 3b.[83] HAADF STEM tomography identified the overall morphology of the dumbbell-like nanoparticle, comprising a Co-based nanorod (ca. 80 nm long) with an Fe-based cubic patch selectively deposited at each nanorod tip (ca. 20 nm diameter). However, the small difference in atomic number between Co and Fe made it difficult to distinguish the elemental distribution by HAADF STEM alone. Moreover, it is well-known that CoFe intermixed alloys can readily form but cannot be identified without a chemically sensitive spectroscopy technique. EDXS tomography showed a well-defined elemental separation between the Co nanorod and the cubic Fe tips. A detailed understanding of this complex structure was used to explain SQUID magnetometry measurements and to understand structure-magnetic anisotropy and exchange-coupling phenomena.

An example of enhanced sample complexity is the recent report by González-Rubio *et al.*[88] The study investigated synthetic routes to build a chiral dendritic (Au or Pt) surface topology onto pre-formed Au nanorods, so as to induce unique optical and enantioselective (chiroptical) behavior. Nanostructures with chiroptical properties are notoriously challenging to synthesize and have exciting applications related to enantioselective chemical sensing, photocatalysis and photothermal therapies.[93,94] González-Rubio *et al.* investigated the elemental distribution of Au@Pt chiral nanorods using HAADF STEM combined with EDXS tomography characterization. Again, HAADF STEM tomography by itself was not sufficient since the

difference in atomic number Z between Au and Pt was too small. The HAADF-EDXS

multimode tomography, presented in Figure 3c, showed that the Pt chiral coating is very regular

around the Au core and highlighted different dimensions of Pt dendrites compared to the

monometallic Au chiral counterpart. From a detailed understanding of elemental distribution

and chiral morphology in 3D, crucial structure-composition-property relationships can be

uncovered to direct future multimetallic chiral nanoparticle design for optimized chiroptical

behavior.
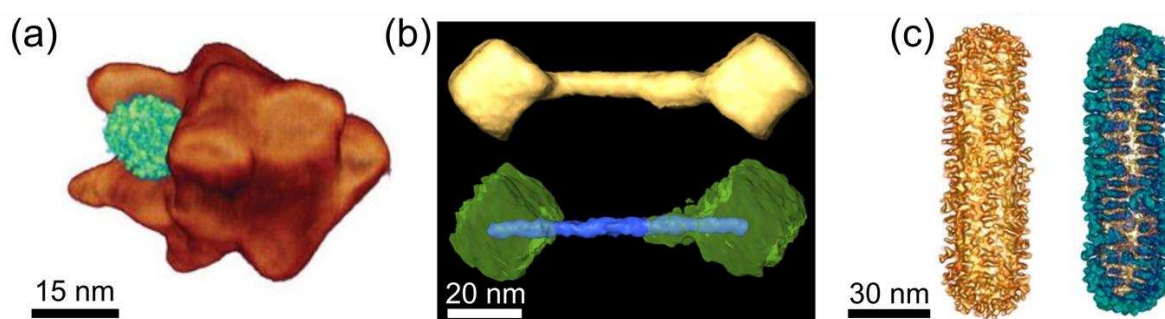
Figure 3. (a) EDXS tomography reconstruction of a Fe_3O_4-Au janus NP (Fe: green, Au: bronze).[92] (b) HAADF STEM and EDXS tomography reconstructions of CoFe dumbbells displaying a Co nanorod core (blue) and Fe growth at the nanorod tips (green).[83] (c) HAADF STEM and EDXS tomography reconstructions of Au@Pt dendritic chiral nanoparticles (Au: gold, Pt: green).[88] Reproduced with permission.

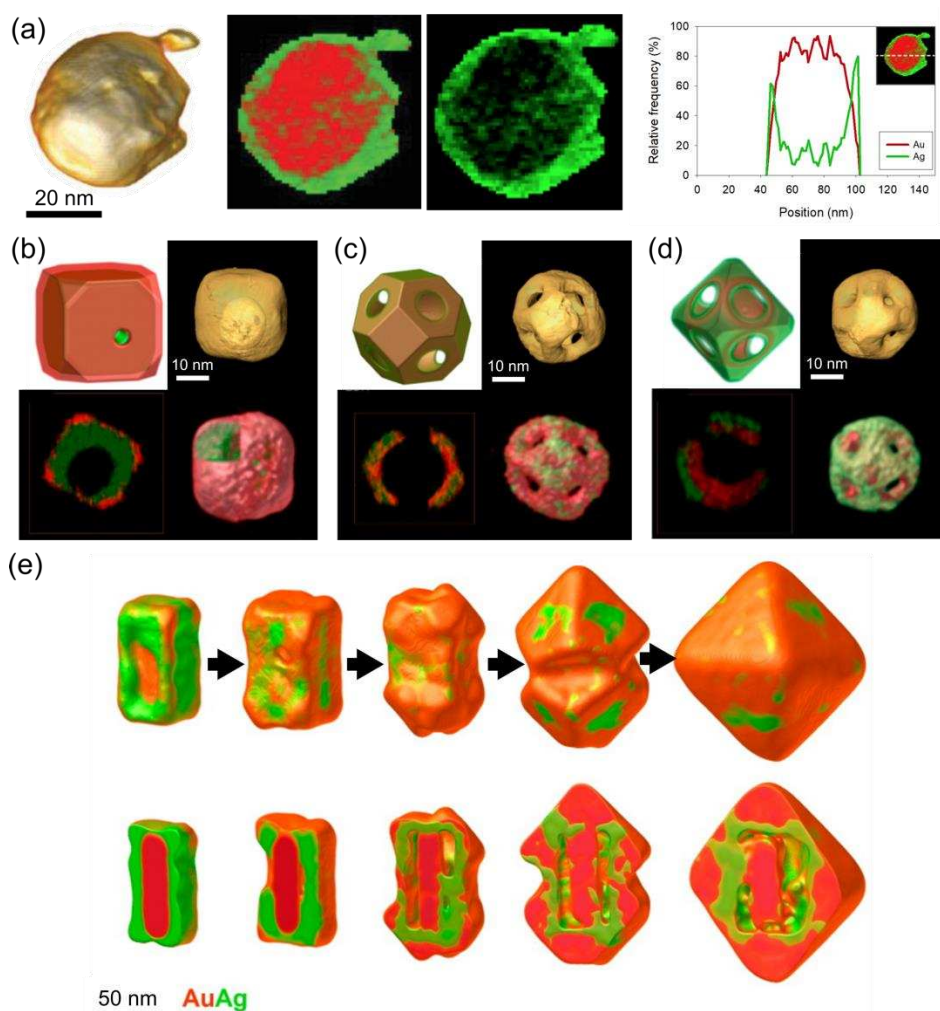### 2.2.3 EDXS tomography for the investigation of alloy formation

Intermixed alloys can be directly synthesized during NP growth, however methods such as co-

precipitation can be difficult to control, leading to pseudo-core@shell arrangements or mixtures

of monometallic and phase-separated NPs. Alternatively, a stepwise synthetic strategy starting

with a monometallic core followed by overgrowth with a secondary element can yield superior

control over the final NP composition.[95–98]

Blommaerts *et al.* investigated the extent of alloying within AuAg NPs prepared by the

Turkevich method using EDXS tomography.[99] The Turkevich method is based upon the co-

reduction of Ag and Au salts by citrate ions and the elemental distribution within the resulting nanoparticles is still a topic of debate, with some bulk phase analysis suggesting a completely disordered alloy structure[100] whereas others reported a core@shell distribution of the elements.[101] EDXS tomography of an AgAu NP, shown in **Figure 4a**, shows a hybrid alloying mode known as a pseudo-core@shell morphology. The pseudo-core@shell morphology was evidenced by EDXS tomography orthoslices through the center of the NP, with extracted intensity line profiles showing a clear abundance of Ag and Au at the surface and the core, respectively, with no clear and abrupt interface.

On the other hand, the galvanic replacement reaction is a prime example of a multistep synthetic route using sacrificial nanoparticle templates and Kirkendall effects for the preparation of hollow, porous and multimetallic metal NPs.[102, 103] The resulting structures are usually known as nanocages or nanorattles and their composition, elemental distribution, morphology, size of internal void, and shell thickness have a profound impact on the material's physical properties. For example, the catalytic activity of AgAu hollow nanospheres for a three-component coupling reaction to form propargylamine was strongly dependent upon composition and elemental distribution.[104] Therefore, a fundamental understanding of the galvanic replacement mechanism is key to control the resulting nanomaterial properties and to design optimized nanoarchitectures for enhanced performance. Goris *et al.* identified a series of key mechanistic insights when monitoring the galvanic replacement of Ag nanocubes by Au, using EDXS tomography.[105] This study uncovered mechanistic information beyond 2D imaging, as elemental mapping studies showed that a thin Au shell can be grown onto the surface of the Ag sacrificial template, thereby protecting remaining Ag from further oxidation (see Figure 4b). 3D morphology investigations enabled the visualization of characteristic 'pinholes' formed at the cube's face within the Au shell. Interestingly, the ability to obtain elemental distribution information from inside of the NP revealed Au coating around the pinhole, which prevented its

further growth and allowed a cubic morphology to be maintained whilst the internal Ag volume of the shell was being etched away. By increasing the Au^{3+} concentration further, Au was deposited on the inside of the hollow nanocage and induced alloy formation and a transition in morphology (Figure 4c) from {100} surface faceting (cubic) to {111} surface facets (truncated octahedral morphology). Finally, using an even larger amount of Au^{3+}, the reshaping process was completed to form octahedra with sharp {111} facets displaying large holes in the center of each facet (Figure 4d). Due to the complex morphology of these particles, the ability to track this process in 3D was crucial to identify an Ag-dominant shell inside the particle.[105]

Figure 4. (a) Investigation of Turkevich AuAg alloy preparation by EDXS tomography displaying HAADF reconstruction, orthoslices and linescan intensity profiles of Ag and Au signal intensities (Au in red, Ag in green), to show elemental mixing and a pseudo core@shell architecture.[99] (b-d) visualizations of EDXS tomography results[105] displaying model structures (top left), HAADF STEM tomography reconstructions (top right), orthoslices of the structure showing internal elemental distributions (bottom left) and EDXS reconstructions

(bottom right). (b) to (d) show morphology and composition progression with increasing HAuCl4 concentration. (e) Quantitative EDXS tomography study showing the transformation of Au@Ag nanorods into octahedral nanorattles at discrete reaction stages upon increasing HAuCl4 concentrations (above) and cross sections through the reconstructions, to display the internal structure of the same NPs (below).[106] Reproduced with permission.

EDXS tomography investigations of galvanic replacement in the AgAu system were extended by Polavarapu *et al.*, to consider the role of the initial template morphology upon the final nanorattle architecture[106] This study supported the design of novel nanocage architectures by enabling the characterization of morphological changes and facet evolution, to investigate the influence of mild reducing agents during galvanic replacement of Au@Ag nanorods. Figure 4e shows representative 3D elemental distribution studies throughout the galvanic replacement process. Upon initial exposure to HAuCl4, the Ag shell was partially eroded through a galvanic replacement mechanism, which was evidenced by grooves forming on the Ag surface and a small but measurable Au shell that could only be reliably visualized by 3D characterization. Interestingly, by considering non-spherical NPs, fundamental trends in structure-reactivity correlations were discovered, showing that during the initial stages of the galvanic replacement Au selectively deposits at the corners of rectangular cuboid Ag seeds through an alternative mechanism to the additive-free galvanic replacement. This facet-reactivity observation provides the first experimental evidence of corners > edges > facets reactivity trends for a cuboid structure and potentially impacts a wide range of chemical transformations beyond the galvanic replacement reaction.[106]

2.2.4 Quantitative EDXS tomography

Uncovering subtle changes in reaction mechanisms and reaction kinetics often requires tracking the composition and morphology of nanomaterials during the reaction process in a quantitative manner. Unfortunately, for quantitative EDXS tomography analysis, remaining shadowing effects pose again a significant challenge. A potential solution was reported by Zanaga *et al.*,[79]

through a compensation strategy, which is summarized in **Figure 5**. In contrast to EDXS intensity normalization, elemental EDXS maps based on the ratio of a target element to the sum of every element within the spectrum were used as an input for tomography reconstruction. In this manner, the extent of shadowing at each angle contained its own internal standard, specific to the experiment rather than relying on external holder calibrations.[80] However, sample thickness information was lost during the generation of such quantitative EDXS maps, which would be necessary to fulfill the projection requirement for tomography reconstruction. Therefore, chemically quantified projection images were constructed using sample thickness information extracted from HAADF STEM tomograms, acquired simultaneously from the same particle, which are not influenced by shadowing effects (except for the usual missing wedge artifact).
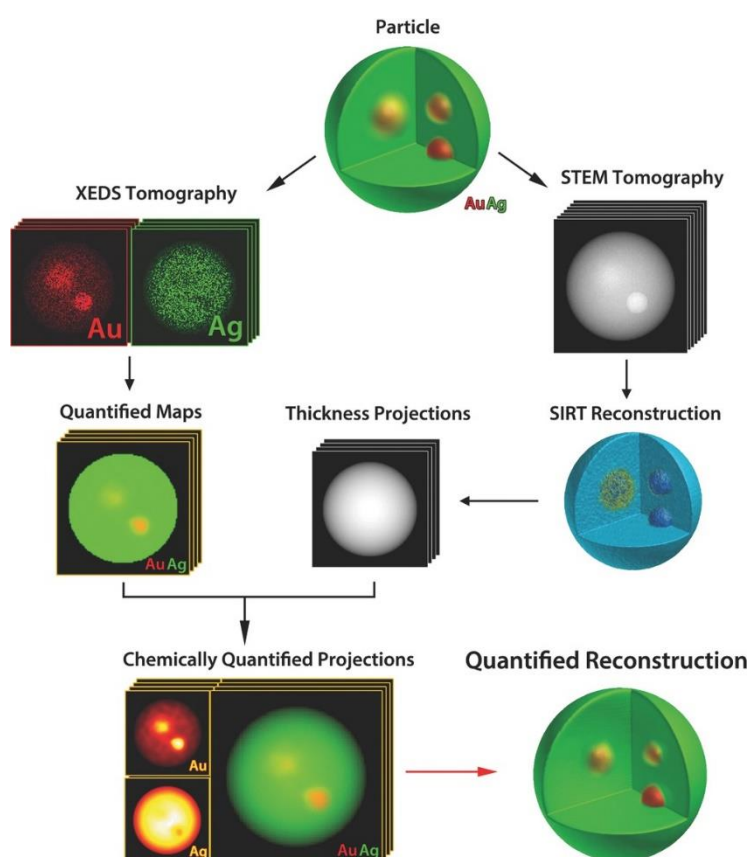
Figure 5. A schematic representation of the principal steps of quantitative EDXS tomography proposed by Zanaga *et al.* illustrated on a simulated particle of Au and Ag. Reprinted with permission.[79]

This quantitative EDXS tomography technique was also used for the 3D quantitative elemental distribution analysis of AgAu nanorattles in Figure 4, to investigate elemental concentration gradients through the nanorattle shell. The study revealed that the internal surface of the shell consisted of an AuAg alloy (Ag content: 20% - 50%), rather than a monometallic Ag surface, which again impacts the observed physical properties of such nanorattles. The study indicated that the reaction between a monometallic Ag template NP and Au^{3+} ions proceeded through a galvanic replacement mechanism, as expected. However, as the composition of the particles evolved to incorporate a significant Au content ($Ag_{40}Au_{60}$), further NP transformations were dominated by a seeded-growth mechanism evidenced by compositional changes and elemental distribution analysis enabled by EDXS tomography.[106]

The transition from a core@shell to an intermixed alloy structure can be achieved through thermal annealing at moderate or high temperatures in the dry state. However, plasmonic NPs have the potential to undergo heat-induced alloying in aqueous media, unlike conventional thermal treatments in the solid state. The ability to alloy while the NPs are dispersed in solution is of great interest toward using alternative alloying mechanisms to conventional thermal treatment, and may also prevent NP sintering, e.g. removing the need for growing a protective SiO_2 shell prior to thermal treatment.[31] An example is the work by González-Rubio *et al.*, who tracked the influence of femtosecond laser irradiation on core@shell Au@Ag nanorods, to investigate the potential of thermal relaxation to induce alloying.[107] Au@Ag NRs were thus irradiated with 2.3, 6.1 and 33.2 J m^{-1} fluxes. Irradiation resulted in the selective removal of Ag from the tips of the core@shell NRs, leaving an unexposed Au core (2.3 J m^{-1}), followed by the nanorod tip becoming increasingly rounded into an ellipsoidal morphology (6.1 J m^{-1}), and finally, upon extreme irradiation, the formation of spherical NPs no longer displaying any evidence of a core@shell arrangement (33.2 J m^{-1}). Crucially, upon 2.3 J m^{-1} flux irradiation, EDXS tomography revealed that Ag initially located at the NR tips did not alloy with the

exposed Au core's tips, but had either re-located to the remaining Ag shell or was dissolved/etched into the aqueous solution during irradiation. Upon 6.1 J m^{-1} irradiation, EDXS tomography showed clear evidence of alloying, with a distinctively thinner monometallic Au shell, showing the possibility to achieve a controlled annealing event using light rather than conventional heat. Importantly, the extent of alloying extracted from 2D EDXS mapping was found to be misleading, illustrating the importance of investigating reactions of NPs with complex morphologies and the corresponding elemental distributions in 3D.

2.3 EELS Tomography

So far, we have addressed the importance of understanding morphology and elemental distribution within complex nanoarchitectures. However, the physical and chemical properties of nanoparticles can be influenced by other parameters as well. For example, metals with multiple accessible oxidation states have the potential to display various such oxidation states, even within a single particle, including surface- or facet-selective valency. A prototypical case is Fe, which displays drastically different magnetic properties between the zero-valent (metallic) state and oxides such as Fe_3O_4 (mixed Fe^{2+}/Fe^{3+}) or Fe_2O_3 (Fe^{3+}). Modern nanoparticle synthesis techniques have gone beyond morphology and composition control, toward a pre-designed and sometimes variable oxidation state: for example, partially oxidized $Fe@Fe_3O_4$ for combined biomedical imaging and magnetic hyperthermia treatment.[108,109] Furthermore, a simple variation in the choice of precursor or surfactant during synthesis may be sufficient to tailor the oxidation state of small metal nanoparticles, aiming at an optimized performance in e.g. catalysis or biomedical applications. Another example is found in ceria (CeO_2 or CeO_{2-x}) NPs, which display non-homogeneous or even facet-selective oxidation state variations (Ce^{4+}, Ce^{3+}) within the same particle, again affecting the material's properties. Therefore, understanding oxidation state distributions within complex CeO_2 NPs is imperative

to elucidate oxidation state-dependent physical properties that impact a broad range of materials science applications including fuel cells, automotive devices,[110] and heterogeneous catalysis.[111]

A challenge associated with the above examples thus involves characterizing not only composition but also oxidation state variations throughout single particles. Even further, when introducing variable oxidation states in nanostructures with a complex morphology, a complete understanding of the composition and properties can only be achieved when this information is gained in 3D.

Electron energy loss spectroscopy (EELS) is a complementary spectroscopy technique to EDXS for the elemental characterization of nanomaterials. Both EDXS and EELS consider the same core-loss ionization process, which is induced by the electron beam. EDXS detects X-ray emission from the sample upon ionization, whereas EELS measures the electron beam energy after interacting with the sample.[112,113] As the ionization process is an inelastic scattering interaction between sample and electron beam, the energy difference between the scattered electron beam and the incident beam can be used to identify the elements present in the sample. The physical mechanism behind EELS measurements provides a substantial advantage when compared to EDXS for identification of light elements (e.g. Li) since the signal intensity is not restricted by the X-ray fluorescence yield. Moreover, post-specimen electrons can be separated by their energy with a high selectivity using a magnetic prism which enables subtle changes in energy (relating to the ease of atomic ionization, known as ionization energy (IE)) to be accurately measured. The IE of an atom/ion relies strongly on its oxidation state and local chemical bonding, therefore EELS is not limited to elemental identification, but can also be used to probe oxidation state and local chemical environments.[114] The subtle changes in ionization energy and the interpretation of the fine structure of the ionization edge are known

as energy loss near edge structure (ELNES) analysis and require independent reference spectra from known samples to perform an accurate fitting analysis.[115] EELS can additionally go beyond conventional characterization of elemental distribution or oxidation state and be used to directly measure single-particle behavior and physical properties such as surface plasmon modes (plasmon or LSPR mapping) which is discussed in more detail in section 2.3.3.

The experimental acquisition and quantitative analysis are significantly more complex for EELS compared to EDXS, due to asymmetry in signal background and ionization edge shape. Significant background signals may originate from abundant low-energy excitations, and the complexity of this additional information gets incorporated within the edge profile. In addition, not all reference spectra are available and potentially interesting features within experimental datasets that are not present in the reference data set can be easily overlooked.[116] EELS processing is especially complex for thick samples > 50 – 100 nm because of the increased probability of multiple scattering events. A practical consideration when comparing EDXS and EELS to be incorporated into tomography experiments is hardware accessibility. Generally, EDXS is more often available within mid-range microscopes than EEL spectrometers are. Furthermore, several applications that we discuss below require energy resolutions that cannot be reached without using a monochromator, such as those found in high-end aberration corrected microscopes.

2.3.1 Considerations for EELS tomography

EELS mapping (much like EDXS mapping) is beholden to poor SNRs, still highly time consuming, and requires higher electron beam intensities (e.g. 150 pA screen currents), compared to HAADF STEM equivalents (50 pA). Therefore, in the application of EELS tomography, sample stability becomes a key consideration. In addition, the energy resolution

required to extract valence states of an element enforces stringent restrictions in terms of acceptable energy dispersion (eV/channel), for fine-structure details to be resolved. A reduced energy dispersion in turn restricts the measurable energy range, for example, by reducing the dispersion from 1 eV/ch to 0.5 eV/ch, the measurable energy range is halved, consequently doubling the achievable energy resolution. A reduced energy range additionally restricts the number of elements one can measure simultaneously. Therefore, if multiple elements are to be mapped in 3D, several acquisitions might be required at different energy ranges, which is time inefficient and significantly increases beam exposure. However, if valence information is required for one element only (or two elements in close energy proximity), a dual EELS-EDXS approach can be implemented. In this case, selected elements are mapped with oxidation state information from EELS, while simultaneously acquiring EDXS maps where most elements can be detected at the same time. Dual EELS-EDXS is possible thanks to the availability of modern acquisition software.[86]

An important consideration for EELS tomography involves the satisfaction of the projection requirement, which is necessary to reliably reconstruct a signal in 3D. To satisfy this requirement, one must assume only one scattering event per electron. Only in this case can the signal intensity be equated to the number of atoms of the species being measured. As the probability of multiple scattering events increases with sample thickness, the projection requirement can only be satisfied for sufficiently thin samples, unless multiple scattering events can be corrected for.[116] In relatively small specimens, such as small isolated nanoparticles (5 - 10 nm), it can be assumed that beam spreading phenomena are minimized, all scattering events are singular, and the acquired EELS maps are suitable for tomographic reconstruction.[117] Generally, however, absorption factors and multiple scattering events can be corrected for to equate signal intensity to the abundance of each moiety.[116] The extent of absorption depends on the TEM settings used during acquisition, as well as on the size and composition of the

material under investigation. To assess the absorption factor, one usually collects the zero loss peak simultaneously.

Two general strategies are largely accepted to reconstruct EELS tomography data. The first method involves the integration of EELS signal intensity over a selected energy range, corresponding to the intensity of an ionization edge, to generate an energy-filtered image for a given element. This energy-filtered image can be reconstructed into a 3D spectral dataset.[116] We refer to this technique as 'conventional' EELS tomography reconstruction. Alternatively, it is possible to reconstruct 4D spectral volume datasets, where each voxel consists of a full EEL spectrum, by using the entire electron energy loss spectrum as an input. In this case, the EEL spectrum of each voxel is fitted to suitable reference spectra, so as to extract oxidation state distribution information in 3D. There are several advantages to this advanced reconstruction technique compared to its conventional counterparts. Indeed, systematic errors occurring when valency maps are extracted at each angle get accumulated when the maps are used as an input for 3D reconstruction, thereby severely hampering reliable and accurate quantification.[117] Moreover, for 4D reconstructions, a plethora of useful and subtle information from the entire spectrum is retained. On the other hand, reconstructing an entire EEL spectrum rather than extracted elemental maps comes with an increased computational expense and data quality requirements, but modern graphics processing units have made this procedure feasible.[117] HAADF STEM tomography acquisition is typically collected alongside EELS tomography data sets. This is because (HA)ADF STEM images are automatically acquired alongside spectral maps to allow for drift correction and provide a greater spatial resolution and SNR compared to the corresponding spectral image. Therefore, independently reconstructing a (HA)ADF tomogram achieves a more accurate morphology characterization alongside 3D valence mapping at no greater operating or beam irradiation cost.

2.3.2 EELS tomography for oxidation state mapping

As discussed above, the presence, abundance and distribution of valence states within metal NPs can severely affect the physical properties and application performance of nanomaterials. EELS tomography for oxidation state and elemental mapping, combined with HAADF STEM tomography for accurate morphology characterization, are uniquely suited to investigate complex metal NPs displaying variable oxidation states.

Early examples of energy-filtered TEM (EFTEM) tomography have been used to characterize the elemental distribution of Fe within FeAl-Y_2O_3 composites,[118] as well as relative Fe:O ratios within magnetic crystallites.[119] Conventional spectral imaging collects an EEL spectrum from every pixel, whereas EFTEM collects 2D images of 'energy-filtered' electrons within a pre-defined energy loss range.[120] After these early EFTEM tomography breakthroughs, conventional EELS tomography has become more accessible due to improved energy filters and increased computing power,[121] which enabled e.g. the characterization of elemental distributions in AlSi alloys prepared as a focused ion beam (FIB) needle,[86] or $Fe_xCo_{(3-x)}O_4$ impregnated Co_3O_4 mesoporous particles,[122] to highlight a few examples.

The advancement from elemental distribution mapping to valence state mapping by EELS tomography was demonstrated almost a decade after the original EFTEM tomography experiments by Jarausch et al.,[123] who probed the interface of a W-to-Si contact extracted from a semiconductor device. Using a core loss EELS tilt series displaying the Si $L_{2,3}$, Si's ionization edge could be modelled and used to map three different Si chemical states in 3D. The semiconductor material was prepared into a large and relatively stable column, compared to metal nanoparticles, by FIB milling. Valence state mapping within discrete NPs was later achieved on faceted ceria nanocrystals. In this study, Goris et al. [117] investigated the oxidation

state distribution of Ce ions throughout octahedral CeO$_{2-x}$ NPs by 4D EELS.[117] The motivation

of the study was understanding whether the presence of Ce^{3+} was a facet-selective phenomenon.

The authors compared a perfect octahedral morphology displaying only {111} surface facets

with a truncated octahedral morphology displaying both {111} and {001} facets. Comparing

these two morphologies provided valuable insights, as the {111} facets could be compared with

{001} facets that are typically more active. Shown in **Figure 6** are EELS tomography

reconstructions of Ce^{3+} and Ce^{4+} for both octahedral (Figure 6a-c) and truncated octahedral (d-

f) morphologies. In the case of pristine CeO$_{2-x}$ octahedra, the {111} surface facets displayed a

uniform thickness of Ce^{3+} as a 0.8 $\pm$ 0.2 nm shell (Figure 6b). The extent of Ce^{4+} reduction into

Ce^{3+} could be extracted within the mixed oxidation state shell, showing that 20% - 30% of Ce^{4+}

ions were reduced at the surface (Figure 6c). Interestingly, when compared to the truncated

octahedral morphology, it was found that 50% of Ce ions on the {001} surface were in the

reduced state, in addition to a thicker partially reduced shell of 1.4 $\pm$ 0.2 nm (e-f). Therefore,

this study provided single-particle evidence for the increased reactivity of {001} terminating

facets compared to {111} equivalents, by showing that a facet-selective reduction process (Ce^{4+}

to Ce^{3+}) occurs to a greater extent at the more reactive {001} facets.
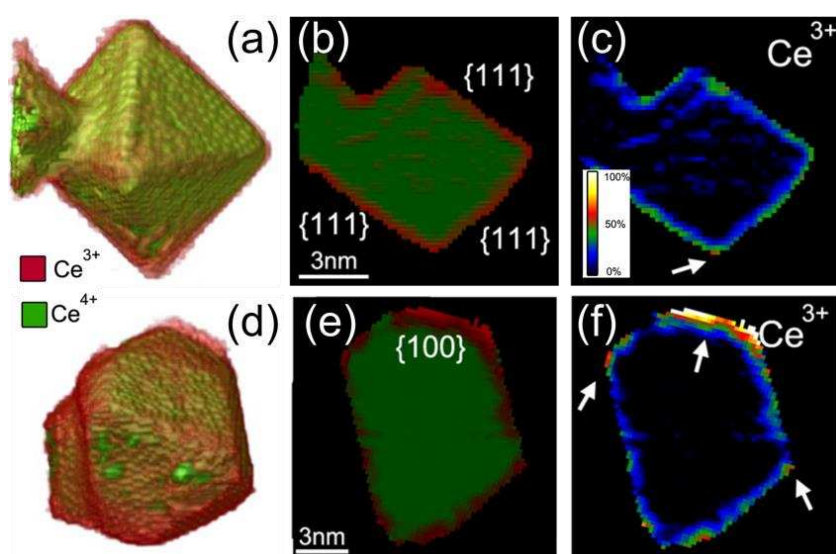
Figure 6. Core loss EELS tomography reconstructions of Ce^{3+} (red) and Ce^{4+} (green) within
octahedral (a) and truncated octahedral (d) CeO$_2$ NPs.[117] (b,e) Slices through the

reconstructions reveal a partially reduced Ce^{3+} surface. (c,f) Quantitative distributions of Ce^{3+} are displayed as a percentage of total Ce signal intensity and show the presence of a greater extent of reduction (more oxide vacancies) at {001} facets, as indicated by white arrows. Reproduced with permission.[117]

In a follow-up study, EELS tomography was applied for the detection of Fe dopants within truncated octahedral CeO_2 NPs.[124] By combining EELS tomography with a prior-knowledge driven direct spectroscopic electron tomography (DS ET) technique, elemental fitting and tomographic reconstruction could be performed simultaneously to disclose the elemental distribution of Fe dopants from spectral maps with limited SNR. With this DS ET reconstruction technique, each chemical component within the EEL spectrum can be fitted with respect to suitable reference spectra during the reconstruction process, within a single step rather than fitting after the entire 4D data set has been obtained. A schematic illustration comparing a conventional EELS tomography reconstruction with a DS ET reconstruction is shown in **Figure 7**a. The approach is particularly beneficial for low SNR data sets (such as those acquired for the detection of dopant-level elements), as systematic errors during peak fitting are not accumulated from each angle of the tilt series during the reconstruction. The sensitivity of this technique enabled the detection of Fe dopants and their 3D spatial distribution, to find the Fe signal localized at the surface of the CeO_2 crystals in addition to internal surfaces created by voids. The valence-sensitivity of EELS additionally enabled the correlation of dopant location with Ce oxidation state and the identification of Fe^{2+} as the origin of the preferential reduction of Ce^{4+} to Ce^{3+} within dopant-rich locations (Figure 7b). The 3D elemental mapping of Ce and Fe in various oxidation states indicated that both Ce and Fe exist simultaneously in their partially reduced states (Ce^{3+} and Fe^{2+}) due to the generation of oxygen vacancies. This challenging study identified a unique dopant-mediated, site-specific strategy that can be used to tailor the oxidation state of Ce within CeO_2.
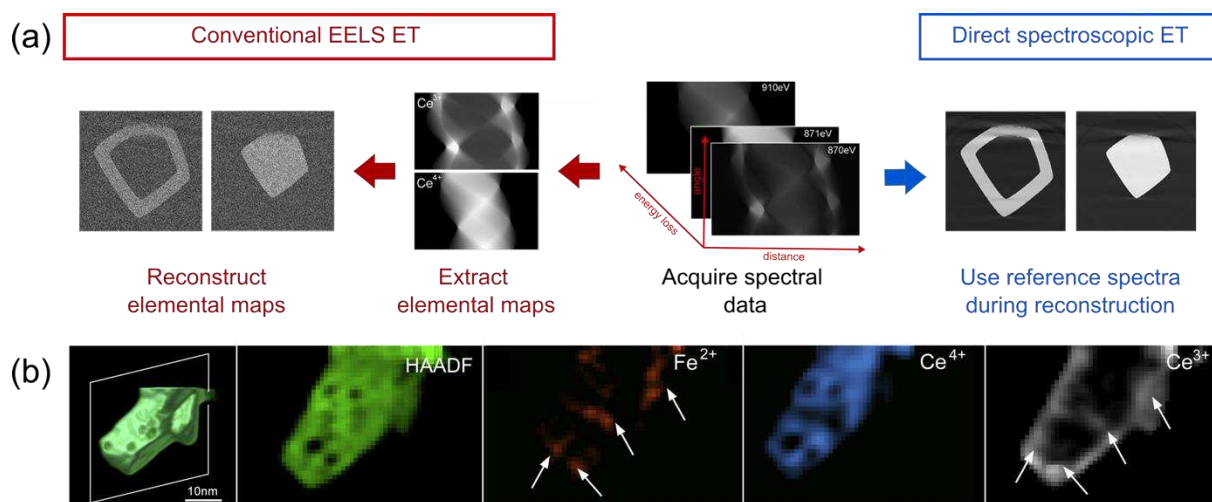
Figure 7. (a) A schematic illustration showing the difference between conventional EELS tomography reconstruction and direct spectroscopic electron tomography (DS ET). (b) DS ET reconstruction of a truncated octahedral Fe-doped CeO_2 nanoparticle, next to extracted orthoslices for HAADF (green), Fe^{2+} (red) Ce^{4+} (blue), and Ce^{3+} (white). White arrows indicate locations with significant Fe dopant concentration, correlating with a high abundance of Ce^{3+}. Adapted with permission from reference.[124]

CeO_2 is an important and widely used material displaying variable oxidation states, however it is by no means the only nanomaterial capable of displaying this phenomenon. As explained above, iron displays a broad range of accessible valence states (Fe^0, Fe^+, Fe^{2+} and Fe^{3+}) which can be distinguished by ELNES analysis due to characteristic fine structures of ionization edges. Iron and iron oxides are vital metal and metal oxide nanoparticles, with applications including (electro)catalysis,[125] nanomedicine,[126] and plasmonics.[127] The valence of Fe within Fe-based nanoparticles is paramount and perhaps even more relevant than morphology, surface faceting and size, regarding their physical properties and potential applications. For instance, FeO is metastable (tending to disproportionate to a higher oxide and Fe metal) and each crystal structure displays drastically different saturation magnetization characteristics in the superparamagnetic state.[128, 129] The combination of mixed Fe oxides into a heterostructure (such as a core@shell arrangement) can lead to exchange coupling in the nanoscale and provide unusual magnetic behavior that can be difficult to correlate to a NP structure unless the complex architecture of the nanocomposite is clearly visualized in 3D.

Torruella *et al.* investigated in 3D the oxidation state variations in magnetic core@shell FeO@Fe$_3$O$_4$ nanocubes prepared by Fe-oleate decomposition, using core loss EELS tomography.[116] By fitting the sharp Fe L$_{2,3}$ ionization edge (aided by well-defined 'white lines' referred to sharp and intense peaks within the ionization edge of an EEL spectrum due to available p-d electronic transitions) to reference spectra, Fe$^{2+/3+}$ ions could be distinguished, and their spatial distributions mapped in 2D for each tilt angle. Principal component analysis (PCA) was applied, in combination with independent component analysis (ICA), to process the spectra and isolate features that were associated with certain chemical phases (such as oxidation states) within the material. For the projection requirement to be satisfied, the absorption factor was estimated on the basis of simultaneously acquired HAADF STEM images, rather than absorption correction from ZLP collection. In the same report, the need for obtaining a sufficient SNR within the spectrum for accurate quantification was emphasized. The study required relatively high dwell times and electron doses, which lead to a significant accumulation of beam damage to the sample as the tilt series was acquired. Due to the relatively simple cubic morphology of the single particle, a mirror image of the tilt series (-69° to 0°) was imposed to complete the data set. By combining the processed valence 2D coefficient maps at each angle, the desired feature could be reconstructed in 3D through a compressed sensing (CS) reconstruction algorithm. CS is a reconstruction technique based on the principle that key features can be extracted from incomplete data sets when supported by prior knowledge of the sample. A CS approach is beneficial toward overcoming a limited number of projections when faced with restrictions such as sample instabilities or restricted rotation capabilities.[130] However, CS- based reconstruction techniques are an active area of research to ensure reliability and trustworthy quantitative results.[131] Moreover, the utilization of only half of a conventionally accessible tilt range (-69° to 0° compared to -80 to + 80 °) becomes increasingly problematic as the NPs morphology or elemental/valence distribution becomes more complex or asymmetric.

The visualization of valence information in 3D for this complex mix-valence composite structure enabled several key findings. An average overall Fe_3O_4 shell with a thickness of 9 nm was identified, which entirely encapsulated a larger, 28 nm edge-length FeO core. Moreover, it was possible to confirm that the shell predominantly contained Fe^{3+}, while a smaller but distinguishable signal from Fe^{2+} was also present.
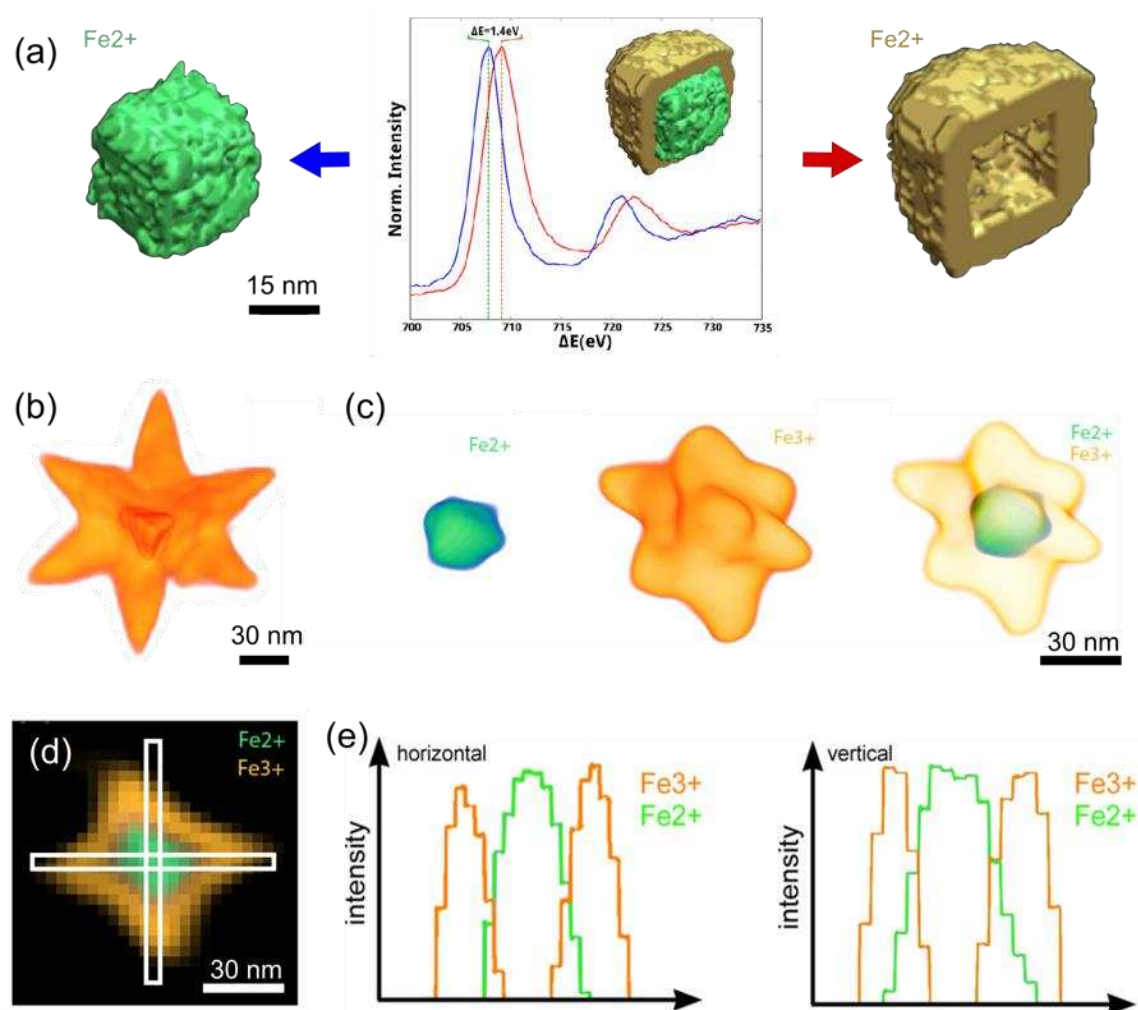
Figure 8. (a) EELS tomography reconstruction of Fe^{2+} (green), Fe^{3+} (yellow) and EEL spectrum of the Fe $L_{2,3}$ ionization edge, showing the energy shift from the core (blue) and the shell (red). (b) HAADF STEM tomography reconstruction of an FeO@Fe_xO_y octapod. (c) EELS tomography reconstruction of Fe^{2+} (green), Fe^{3+} (yellow), and overlayed Fe^{2+} and Fe^{3+} signals. (d) Orthoslice of Fe^{2+} and Fe^{3+} signals from the same octapod displayed in c. White bars indicate the location of linescan intensity profiles. (e) Horizontal and vertical linescan intensity profiles. Reproduced with permission.[116, 129]

Feld *et al.* used 4D EELS tomography to investigate FeO@Fe$_x$O$_y$ NPs prepared by Fe-oleate decomposition, displaying a complex octapod morphology (Figure 8b).[129] Although the particles were initially prepared as FeO, limited surface oxidation upon atmospheric exposure generated a complex heterostructure displaying multiple valence states within the octapods. Both the core and the shell were found to contain Fe^{2+} by monochromated ELNES analysis in 2D, with an abundance of Fe^{3+} at the particle surface and octapod tips, indicating a maghemite (Fe$_2$O$_3$) structure. However, 3D characterization was required to assess whether Fe^{3+} signals originate from the core of the octapod or from the oxidized shell located above and below the core region. Monochromated core loss EELS tomography, combined with DS ET reconstruction,[124] showed a clear dominance of Fe^{3+} at the octapod surface confirming an Fe$_2$O$_3$ shell (Figure 8 c) and a central core consisting solely of wüstite (FeO). However, Fe valency orthoslices through the reconstruction (Figure 8d-e) and their extracted linescan intensity profiles did not reveal a standard core@shell profile. Alternatively, the reconstruction showed a blurred interface between both oxide phases, with a gradual decrease in Fe^{3+} towards the particle core. This finding gives unique mechanistic detail of FeO oxidation with an intermediate interface between 'core' and 'shell', with the 2:1 Fe^{3+}:Fe^{2+} mixed valency required for a magnetite (Fe$_3$O$_4$) structure. From these results, it can be proposed that FeO oxidation occurs through intermediate mixed valence oxides, before finally achieving Fe$_2$O$_3$. The 3D EELS experiments show single-particle evidence of a mixed oxide species within a complex nanostructure which is in agreement with bulk-phase Mössbauer spectroscopy experiments.[132]

2.3.3 EELS tomography for LSPR mapping

Localized surface plasmon resonance (LSPR) modes can be excited in plasmonic nanostructures using an electron beam of the appropriate energy, instead of visible or near IR light.[133] Implementation of this technique in modern transmission electron microscopes has

enabled a greater understanding of plasmonic nanoparticles at a single-particle level. Although alternative techniques can be used to achieve single-particle optical studies, such as dark field optical microscopy[134] or scanning near-field optical microscopy (SNOM),[135] plasmon mapping using EELS (which can be achieved in combination with cathodoluminescence measurements to identify the type of plasmon mode)[136] enables the direct visualization of LSPR modes within different NP morphologies. The resonance frequencies of LSPR modes can be directly extracted from a low loss EEL spectrum during incident electron beam exposure, which directly excites both surface and bulk metal plasmons.[137] Several LSPR mapping studies have been performed in 2D, which provided impressive insights to the materials science community.[133, 138] Typically, monochromated EELS point scans, linescans,[139] or spectral maps [140,141] are acquired close to the ZLP (~1 – 10 eV). The resulting energy loss that is associated with the different LSPR modes (during kinetic energy loss of the electron beam during plasmon excitation) can be observed within the background-subtracted low-loss spectrum close to the ZLP, from which plasmon maps can be obtained by selecting and mapping an energy range associated with the energy loss of a specific mode. LSPR mapping in 2D becomes particularly challenging when the NP morphology becomes more complex and asymmetric, requiring the visualization of modes that are excited at different NP orientations. However, it is important to note that low loss EELS signals such as surface plasmon excitations do not strictly follow the projection requirement required for tomography reconstruction,[120] and several groups have reported the systematic and unavoidable variation of low loss signal with collection angle.[123,142]

Nicoletti *et al.* mapped LSPR modes of Ag nanocubes (c.a. 100 nm) based on restricted tilt ranges (-60° to 15° and +15° to +60° or $\pm$ 60°, where only -60° to 0° was used due to the near perfect symmetry of the nanocube) to prevent beam damage of the sample and buildup of carbonaceous contamination.[143] Plasmon modes occur close to the ZLP (1-4 eV) for Ag and

the 'fine structure' of this energy region presents overlapping modes that require a deconvolution process to be separated. Five distinct EELS-LSPR excitations were used as an input for a CS-based reconstruction algorithm to accommodate for restrictions in tilt angle acquisition, as discussed above for $FeO@Fe_3O_4$ core loss mapping.[116] The resulting 3D LSPR modes are displayed in **Figure 9**a. The ability to visualize LSPR modes in 3D is a cornerstone achievement toward complete understanding and a crucial first step toward LSPR manipulation through the targeted development of complex plasmonic NP morphologies. More recently, plasmon mapping combined with extensive computational simulations to generate simulated eigenmodes has enabled additional information to be extracted from EELS data. Examples include charge density maps for silver bipyramids on an MoO_3 support[144] and photonic local density of states (LDOS) of plasmon-coupled Ag nanostructures,[145-146] shown in Figure 9b and 9c, respectively.
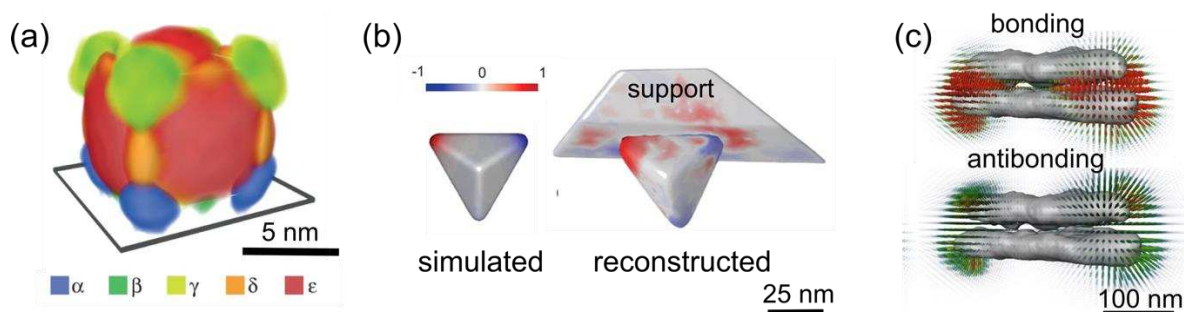
Figure 9. (a) Reconstructed LSPR modes of an Ag nanocube, showing intense substrate-induced polarization of α toward the substrate and subsequent enhanced intensity of β and γ at the top corners due to substrate-induced mode splitting (where α - ε are used to label the different LSPR modes).[143] (b) Simulated and experimental low loss STEM EELS surface charge tomography reconstruction of a silver bipyramid on a MoO_3 support.[144] (c) Reconstructed photonic localized densities of states around Ag triangular prism dimers, displayed as pencils where colour and length display the magnitude and orientation at areas where the LDOS is maximum.[146] Reprinted with permission.

2.4 Conclusion and outlook

Throughout this review, we have discussed how multimodal tomography is driving our knowledge of complex metal and metal oxide nanoparticles and our understanding of structure-property relationships to an unprecedented level, within complex nanoarchitectures. We have considered how multimode tomography such as HAADF-LAADF combinations can be used for the visualization of defects and to identify the presence and role of seed nanoparticles in twinned nanocrystal synthesis. Furthermore, we have discussed the use of EDXS tomography to simultaneously elucidate elemental distributions and morphology in 3D within multimetallic systems and how this technique can be used to track reaction processes such as the galvanic replacement reaction and irradiation-induced alloying, to reveal composition dependent reaction mechanisms. Finally, we discussed how EELS tomography has been used to measure morphology, composition, and metal valence state mapping in 3D to identify facet selective reduction and surface selective oxidation processes within complex faceted nanoparticles. Moreover, key studies were summarized where EELS tomography was used to measure the physical properties of a nanomaterial, such as localized surface plasmon resonances, to uncover structure-property relationships in 3D.

The next challenge will be to optimize these approaches for subsequent investigations:

(i) Although metal NPs are not usually considered to be beam-sensitive, the collection of an entire tilt series (or multiple tilt series) results in a considerable increase in beam exposure compared to 2D measurements. The total electron beam exposure during the acquisition of a tilt series may be sufficient to physically alter a NP's morphology, to induce changes in elemental distributions and even alter the oxidation state of metal atoms. Reducing the time needed to acquire a full tomography data set will help minimize beam damage. The combination of fast ET with multimodal approaches is therefore of great promise.[32]

(ii) *In situ* TEM studies (e.g. tomography during heating) often requires images of the *same* NP to be re-acquired at various stages of the reaction. Therefore, extra care is needed to ensure that any changes within NP structure are a consequence of the reaction, rather than repeated beam exposure. It is not always possible to avoid beam-induced artifacts during an *in situ* experiment, however reduced beam exposure from faster acquisition times may help reduce beam-induced artifacts. Moreover, tracking multiple NPs in 3D and re-acquiring a new tomogram for each NP at various stages of the reaction is incredibly time consuming. Therefore, the required time severely restricts the number of NPs, sampling steps, and therefore overall reaction complexity in a single experiment. These restrictions are especially limiting when one of the acquisition modes is spectroscopy based, such as e.g. EDXS. Skorikov *et al.* have recently developed a dose-minimizing technique based upon a deep-learning algorithm within a U-net deep neural network architecture, to overcome noisy EDXS data.[147] Through the use of this purposely designed denoising strategy that incorporates prior knowledge about the sample, a drastically improved tradeoff between signal intensity and electron dose can be achieved, even when compared to more conventional EDXS denoising strategies. Although Skorikov's investigation is not the first example of this technique applied to EDXS tomography datasets, it does represent the first method to consider a large variety of NP structures and morphologies needed to be used as a reliable and representative general approach to optimize dose-efficient EDXS acquisition for a variety of NP systems. We propose that, U-net restoration will be applied to EELS data sets in the near future upon sufficient neural network training with relevant EELS datasets. The use of U-net EELS studies is an exciting future prospect to consider a complete tilt series on beam sensitive samples and more complex asymmetric morphologies during core loss and plasmon mapping in 3D.

REFERENCES

1   A. K. Salem, P. C. Searson and K. W. Leong, *Nat. Mater.*, 2003, **2**, 668–671.

2   P. C. Ray, *Chem. Rev.*, 2010, **110**, 5332–5365.

3   D. Jimenez de Aberasturi, A. B. Serrano-Montes, J. Langer, M. Henriksen-Lacey, W. J. Parak and L. M. Liz-Marzán, *Chem. Mater.*, 2016, **28**, 6779–6790.

4   S. Szunerits, J. Spadavecchia and R. Boukherroub, *Rev. Anal. Chem.*, 2014, **33**, 153–164.

5   G. González-Rubio, T. M. De Oliveira, T. Altantzis, A. La Porta, A. Guerrero-Martínez, S. Bals, L. Scarabelli and L. M. Liz-Marzán, *Chem. Commun.*, 2017, **53**, 11360–11363.

6   K. J. Jenkinson, A. Wagner, N. Kornienko, E. Reisner and A. E. H. Wheatley, *Adv. Funct. Mater.*, 2020, **2002633**, 3–9.

7   A. Sánchez-Iglesias, K. Jenkinson, S. Bals and L. M. Liz-Marzán, *J. Phys. Chem. C*, 2021, **125**, 23937–23944.

8   S. Cheong, J. D. Watt and R. D. Tilley, *Nanoscale*, 2010, **2**, 2045.

9   S. Bals, B. Goris, L. M. Liz-Marzán and G. Van Tendeloo, *Angew. Chemie - Int. Ed.*, 2014, **53**, 10600–10610.

10   P. R. Sajanlal, T. S. Sreeprasad, A. K. Samal and T. Pradeep, *Nano Rev.*, 2011, **2**, 5883–5945.

11   P. D. Cozzoli, E. Snoeck, M. A. Garcia, C. Giannini, A. Guagliardi, A. Cervellino, F. Gozzo, A. Hernando, K. Achterhold, N. Ciobanu, F. G. Parak, R. Cingolani and L. Manna, *Nano Lett.*, 2006, **6**, 1966–1972.

12   P. A. Midgley and M. Weyland, *Ultramicroscopy*, 2003, **96**, 413–431.

13   P. A. Midgley and R. E. Dunin-Borkowski, *Nat. Mater.*, 2009, **8**, 271–280.

14   S. Bals, G. Van Tendeloo and C. Kisielowski, *Adv. Mater.*, 2006, **18**, 892–895.

15   E. Bladt, R. J. A. van Dijk-Moes, J. Peters, F. Montanarella, C. de Mello Donega, D. Vanmaekelbergh and S. Bals, *J. Am. Chem. Soc.*, 2016, **138**, 14288–14293.

16   M. J. Schnepf, M. Mayer, C. Kuttner, M. Tebbe, D. Wolf, M. Dulle, T. Altantzis, P. Formanek, S. Förster, S. Bals, T. A. F. König and A. Fery, *Nanoscale*, 2017, **9**, 9376–9385.

17   B. Goris, A. De Backer, S. Van Aert, S. Gómez-Graña, L. M. Liz-Marzán, G. Van Tendeloo and S. Bals, *Nano Lett.*, 2013, **13**, 4236–4241.

18   S. Bals, M. Casavola, M. A. van Huis, S. Van Aert, K. J. Batenburg, G. Van Tendeloo and D. Vanmaekelbergh, *Nano Lett.*, 2011, **11**, 3420–3424.

19   S. Gómez-Graña, B. Goris, T. Altantzis, C. Fernández-López, E. Carbó-Argibay, A. Guerrero-Martínez, N. Almora-Barrios, N. López, I. Pastoriza-Santos, J. Pérez-Juste, S. Bals, G. Van Tendeloo and L. M. Liz-Marzán, *J. Phys. Chem. Lett.*, 2013, **4**, 2209–2216.

20   J. E. Wittig, J. Bentley, L. F. Allard and J. Bentley, *Ultramicroscopy*, 2017, **176**, 218–232.

21   M. Radermacher, ed. J. Frank, Springer US, Boston, MA, 1992, pp. 91–115.

22   P. Gilbert, *J. Theor. Biol.*, 1972, **36**, 105–117.

23   T. K. Moon, *IEEE Signal Process. Mag.*, 1996, **13**, 47–60.

24   B. Goris, W. Van den Broek, K. J. Batenburg, H. Heidari Mezerji and S. Bals, *Ultramicroscopy*, 2012, **113**, 120–130.

25   S. Bals, B. Goris, A. De Backer, S. Van Aert and G. Van Tendeloo, *MRS Bull.*, 2016, **41**, 525–530.

26   K. J. Batenburg, S. Bals, J. Sijbers, C. Kübel, P. A. Midgley, J. C. Hernandez, U. Kaiser, E. R. Encina, E. A. Coronado and G. Van Tendeloo, *Ultramicroscopy*, 2009, **109**, 730–740.

27   H. Vanrompay, A. Skorikov, E. Bladt, A. Béché, B. Freitag, J. Verbeeck and S. Bals, *Ultramicroscopy*, 2021, **221**, 113191.

28   V. Migunov, H. Ryll, X. Zhuge, M. Simson, L. Strüder, K. J. Batenburg, L. Houben

and R. E. Dunin-Borkowski, *Sci. Rep.*, 2015, **5**, 14516.

29 H. Vanrompay, E. Bladt, W. Albrecht, A. Béché, M. Zakhozheva, A. Sánchez-Iglesias, L. M. Liz-Marzán and S. Bals, *Nanoscale*, 2018, **10**, 22792–22801.

30 W. Albrecht, E. Bladt, H. Vanrompay, J. D. Smith, S. E. Skrabalak and S. Bals, *ACS Nano*, 2019, **13**, 6522–6530.

31 M. Mychinko, A. Skorikov, W. Albrecht, A. Sánchez-Iglesias, X. Zhuo, V. Kumar, L. M. Liz-Marzán and S. Bals, *Small*, 2021, **2102348**, 1–11.

32 W. Albrecht and S. Bals, *J. Phys. Chem. C*, 2020, **124**, 27276–27286.

33 P. A. Midgley and S. Bals, *Handb. Nanoscopy*, 2012, 253–279.

34 P. Penczek, M. Marko, K. Buttle and J. Frank, *Ultramicroscopy*, 1995, **60**, 393–410.

35 I. Arslan, J. R. Tong and P. A. Midgley, *Ultramicroscopy*, 2006, **106**, 994–1000.

36 N. Kawase, M. Kato, H. Nishioka and H. Jinnai, *Ultramicroscopy*, 2007, **107**, 8–15.

37 X. Ke, S. Bals, D. Cott, T. Hantschel, H. Bender and G. Van Tendeloo, *Microsc. Microanal.*, 2010, **16**, 210–217.

38 K. Jarausch and D. N. Leonard, *J. Electron Microsc. (Tokyo).*, 2009, **58**, 175–183.

39 E. Bladt, D. M. Pelt, S. Bals and K. J. Batenburg, *Ultramicroscopy*, 2015, **158**, 81–88.

40 T. Sanders, A. Gelb, R. B. Platte, I. Arslan and K. Landskron, *Ultramicroscopy*, 2017, **174**, 97–105.

41 P. W. Hawkes, *Electron Tomography: Three dimensional imaging with the transmission electron microscope*, Springer, London, 1st edn., 1992.

42 W. Van den Broek, A. Rosenauer, B. Goris, G. T. Martinez, S. Bals, S. Van Aert and D. Van Dyck, *Ultramicroscopy*, 2012, **116**, 8–12.

43 T. Altantzis, B. Goris, A. Sánchez-Iglesias, M. Grzelczak, L. M. Liz-Marzán and S. Bals, *Part. Part. Syst. Charact.*, 2013, **30**, 84–88.

44 Z. Saghi, X. Xu and G. Möbus, *J. Microsc.*, 2008, **232**, 186–195.

45 T. Altantzis, D. Wang, A. Kadu, A. van Blaaderen and S. Bals, *J. Phys. Chem. C*, 2021, **125**, 26240–26246.

46 N. Winckelmans, T. Altantzis, M. Grzelczak, A. Sánchez-Iglesias, L. M. Liz-Marzán and S. Bals, *J. Phys. Chem. C*, 2018, **122**, 13522–13528.

47 C.-L. Huang, K. Sasaki, D. Senthil Raja, C.-T. Hsieh, Y.-J. Wu, J.-T. Su, C.-C. Cheng, P.-Y. Cheng, S.-H. Lin, Y. Choi and S.-Y. Lu, *Adv. Energy Mater.*, 2021, **11**, 2101827.

48 Q. Lang, W. Hu, P. Zhou, T. Huang, S. Zhong, L. Yang, J. Chen and S. Bai, *Nanotechnology*, 2017, **28**, 484003.

49 T. Lv, Y. Wang, S.-I. Choi, M. Chi, J. Tao, L. Pan, C. Z. Huang, Y. Zhu and Y. Xia, *ChemSusChem*, 2013, **6**, 1923–1930.

50 B. T. Sneed, A. P. Young and C.-K. Tsung, *Nanoscale*, 2015, **7**, 12248–12265.

51 C.-H. Kuo, L. K. Lamontagne, C. N. Brodsky, L.-Y. Chou, J. Zhuang, B. T. Sneed, M. K. Sheehan and C.-K. Tsung, *ChemSusChem*, 2013, **6**, 1993–2000.

52 J. Wu, L. Qi, H. You, A. Gross, J. Li and H. Yang, *J. Am. Chem. Soc.*, 2012, **134**, 11880–11883.

53 B. Goris, S. Bals, W. Van den Broek, E. Carbó-Argibay, S. Gómez-Graña, L. M. Liz-Marzán and G. Van Tendeloo, *Nat. Mater.*, 2012, **11**, 930–935.

54 J. S. Barnard, J. Sharp, J. R. Tong and P. A. Midgley, *J. Phys. Conf. Ser.*, 2006, **26**, 247–250.

55 R. Tovey, D. N. Johnstone, S. M. Collins, W. R. B. Lionheart, P. A. Midgley, M. Benning and C.-B. Schönlieb, *Inverse Probl.*, 2020, **37**, 15003.

56 J. S. Barnard, A. S. Eggeman, J. Sharp, T. A. White and P. A. Midgley, *Philos. Mag.*, 2010, **90**, 4711–4730.

57 J. Kacher and I. M. Robertson, *Philos. Mag.*, 2014, **94**, 814–829.

58 J. D. Smith, E. Bladt, J. A. C. Burkhart, N. Winckelmans, K. M. Koczkur, H. M. Ashberry, S. Bals and S. E. Skrabalak, *Angew. Chemie Int. Ed.*, 2020, **59**, 943–950.

59   L. He, Y. Liu, J. Liu, Y. Xiong, J. Zheng, Y. Liu and Z. Tang, *Angew. Chemie Int. Ed.*, 2013, **52**, 3741–3745.

60   A. Arenas-Vivo, S. Rojas, I. Ocaña, A. Torres, M. Liras, F. Salles, D. Arenas-Esteban, S. Bals, D. Ávila and P. Horcajada, *J. Mater. Chem. A*, 2021, **9**, 15704–15713.

61   G. Zheng, S. de Marchi, V. López-Puente, K. Sentosun, L. Polavarapu, I. Pérez-Juste, E. H. Hill, S. Bals, L. M. Liz-Marzán, I. Pastoriza-Santos and J. Pérez-Juste, *Small*, 2016, **12**, 3935–3943.

62   M. Aghayi-Anaraki and V. Safarifard, *Eur. J. Inorg. Chem.*, 2020, **2020**, 1916–1937.

63   G. Zheng, I. Pastoriza-Santos, J. Pérez-Juste and L. M. Liz-Marzán, *SmartMat*, **2**, 446-465

64   B. Shen, X. Chen, K. Shen, H. Xiong and F. Wei, *Nat. Commun.*, 2020, **11**, 2692.

65   R. F. Egerton, *Microsc. Res. Tech.*, 2012, **75**, 1550–1556.

66   K. Sentosun, M. N. Sanz Ortiz, K. J. Batenburg, L. M. Liz-Marzán and S. Bals, *Part. Part. Syst. Charact.*, 2015, **32**, 1063–1067.

67   K. Song, L. R. Comolli and M. Horowitz, *J. Struct. Biol.*, 2012, **178**, 108–120.

68   M. N. Sanz-Ortiz, K. Sentosun, S. Bals and L. M. Liz-Marzán, *ACS Nano*, 2015, **9**, 10489–10497.

69   G. Zheng, S. de Marchi, V. López-Puente, K. Sentosun, L. Polavarapu, I. Pérez-Juste, E. H. Hill, S. Bals, L. M. Liz-Marzán, I. Pastoriza-Santos and J. Pérez-Juste, *Small*, 2016, 3935–3943.

70   G. Zheng, Z. Chen, K. Sentosun, I. Pérez-Juste, S. Bals, L. M. Liz-Marzán, I. Pastoriza-Santos, J. Pérez-Juste and M. Hong, *Nanoscale*, 2017, **9**, 16645–16651.

71   N. Pazos-Pérez, B. Rodríguez-González, M. Hilgendorff, M. Giersig and L. M. Liz-Marzán, *J. Mater. Chem.*, 2010, **20**, 61–64.

72   J. Watt, S. Cheong and R. D. Tilley, *Nano Today*, 2013, **8**, 198–215.

73   L. R. Hirsch, R. J. Stafford, J. A. Bankson, S. R. Sershen, B. Rivera, R. E. Price, J. D. Hazle, N. J. Halas and J. L. West, *Proc. Natl. Acad. Sci. U. S. A.*, 2003, **100**, 13549–13554.

74   V. Tzitzios, D. Niarchos, M. Gjoka, N. Boukos and D. Petridis, *J. Am. Chem. Soc.*, 2005, **127**, 13756–13757.

75   C. M. Gonzalez, B. Martin and T. Betancourt, *J. Mater. Chem. A*, 2014, **2**, 17574–17585.

76   E. Ha, L. Y. S. Lee, H.-W. Man, S. C. E. Tsang and K.-Y. Wong, *ACS Appl. Mater. Interfaces*, 2015, **7**, 9072–9077.

77   A. Skorikov, W. Albrecht, E. Bladt, X. Xie, J. E. S. Van Der Hoeven, A. Van Blaaderen, S. Van Aert and S. Bals, *ACS Nano*, 2019, **13**, 13421–13429.

78   G. Möbus, R. C. Doole and B. J. Inkson, *Ultramicroscopy*, 2003, **96**, 433–451.

79   D. Zanaga, T. Altantzis, L. Polavarapu, L. M. Liz-Marzán, B. Freitag and S. Bals, *Part. Part. Syst. Charact.*, 2016, **33**, 396–403.

80   T. J. A. Slater, A. Janssen, P. H. C. Camargo, M. G. Burke, N. J. Zaluzec and S. J. Haigh, *Ultramicroscopy*, 2016, **162**, 61–73.

81   T. Scientific, Spectra Ultra S/TEM Scanning transmission electron microscope for imaging and spectroscopy of beam sensitive materials., thermofisher.com/spectra-ultra, (accessed 20 December 2021).

82   P. Schlossmacher, D. O. Klenov, B. Freitag and H. S. von Harrach, *Micros. Today*, 2010, **18**, 14–20.

83   N. Liakakos, C. Gatel, T. Blon, T. Altantzis, S. Lentijo-Mozo, C. Garcia-Marcelot, L.-M. Lacroix, M. Respaud, S. Bals, G. Van Tendeloo and K. Soulantica, *Nano Lett.*, 2014, **14**, 2747–2754.

84   B. Goris, B. Freitag, D. Zanaga, E. Bladt, T. Altantzis, J. Ringnalda and S. Bals, *Microsc. Microanal.*, 2014, **20**, 766–767.

85   P. Burdet, Z. Saghi, A. N. Filippin, A. Borrás and P. A. Midgley, *Ultramicroscopy*, 2016, **160**, 118–129.

86   G. Haberfehlner, A. Orthacker, M. Albu, J. Li and G. Kothleitner, *Nanoscale*, 2014, **6**, 14563–14569.

87   S. Khoee and A. Nouri, in *Design and Development of New Nanocarriers*, ed. A. M. B. T.-D. and D. of N. N. Grumezescu, William Andrew Publishing, 2018, pp. 145–180.

88   G. González-Rubio, J. Mosquera, V. Kumar, A. Pedrazo-Tardajos, P. Llombart, D. M. Solís, I. Lobato, E. G. Noya, A. Guerrero-Martínez, J. M. Taboada, F. Obelleiro, L. G. MacDowell, S. Bals and L. M. Liz-Marzán, *Science.*, 2020, **368**, 1472–1477.

89   S.-H. Hu and X. Gao, *J. Am. Chem. Soc.*, 2010, **132**, 7234–7237.

90   M. D. McConnell, M. J. Kraeutler, S. Yang and R. J. Composto, *Nano Lett.*, 2010, **10**, 603–609.

91   M. Felber and R. Alberto, *Nanoscale*, 2015, **7**, 6653–6660.

92   J. Reguera, D. Jiménez De Aberasturi, N. Winckelmans, J. Langer, S. Bals and L. M. Liz-Marzán, *Faraday Discuss.*, 2016, **191**, 47–59.

93   G. Zheng, J. He, V. Kumar, S. Wang, I. Pastoriza-Santos, J. Pérez-Juste, L. M. Liz-Marzán and K. Y. Wong, *Chem. Soc. Rev.*, 2021, **50**, 3738–3754.

94   H.-E. Lee, H.-Y. Ahn, J. Mun, Y. Y. Lee, M. Kim, N. H. Cho, K. Chang, W. S. Kim, J. Rho and K. T. Nam, *Nature*, 2018, **556**, 360–365.

95   S. Sun, E. E. Fullerton, D. Weller and C. B. Murray, *IEEE Trans. Magn.*, 2001, **37**, 1239–1243.

96   G. Li, W. Zhang, N. Luo, Z. Xue, Q. Hu, W. Zeng and J. Xu, *Nanomaterials*, 2021, **11**, 1926.

97   N. Baig, I. Kammakakam and W. Falath, *Mater. Adv.*, 2021, **2**, 1821–1871.

98   M. Chen, J. P. Liu and S. Sun, *J. Am. Chem. Soc.*, 2004, **126**, 8394–8395.

99   N. Blommaerts, H. Vanrompay, S. Nuti, S. Lenaerts, S. Bals and S. W. Verbruggen, *Small*, 2019, **15**, 1–8.

100   T.-W. Liao, A. Yadav, K.-J. Hu, J. van der Tol, S. Cosentino, F. D'Acapito, R. E. Palmer, C. Lenardi, R. Ferrando, D. Grandjean and P. Lievens, *Nanoscale*, 2018, **10**, 6684–6694.

101   M. A. Uppal, M. B. Ewing and I. P. Parkin, *Eur. J. Inorg. Chem.*, 2011, **2011**, 4534–4544.

102   A. G. M. Da Silva, T. S. Rodrigues, S. J. Haigh and P. H. C. Camargo, *Chem. Commun.*, 2017, **53**, 7135–7148.

103   N. Ortiz and S. E. Skrabalak, *Cryst. Growth Des.*, 2011, **11**, 3545–3550.

104   T. J. A. Slater, A. Macedo, S. L. M. Schroeder, M. G. Burke, P. O'Brien, P. H. C. Camargo and S. J. Haigh, *Nano Lett.*, 2014, **14**, 1921–1926.

105   B. Goris, L. Polavarapu, S. Bals, G. Van Tendeloo and L. M. Liz-Marzán, *Nano Lett.*, 2014, **14**, 3220–3226.

106   L. Polavarapu, D. Zanaga, T. Altantzis, S. Rodal-Cedeira, I. Pastoriza-Santos, J. Pérez-Juste, S. Bals and L. M. Liz-Marzán, *J. Am. Chem. Soc.*, 2016, **138**, 11453–11456.

107   G. González-Rubio, P. Díaz-Núñez, W. Albrecht, V. Manzaneda-González, L. Bañares, A. Rivera, L. M. Liz-Marzán, O. Peña-Rodríguez, S. Bals and A. Guerrero-Martínez, *Adv. Opt. Mater.*, 2021, **9**, 1–9.

108   J. P. Mehta, B. R. Knappett, G. Divitini, E. Ringe, P. A. Midgley, D. Fairen-Jimenez and A. E. H. Wheatley, in *Proceedings of the IEEE Conference on Nanotechnology*, 2019.

109   S. Peng, C. Wang, J. Xie and S. Sun, *J. Am. Chem. Soc.*, 2006, **128**, 10676–10677.

110   E. Aneggi, C. de Leitenburg, G. Dolcetti and A. Trovarelli, *Catal. Today*, 2006, **114**, 40–47.

111   V. V Galvita, H. Poelman, V. Bliznuk, C. Detavernier and G. B. Marin, *Ind. Eng.*

Chem. Res., 2013, **52**, 8416–8426.

112 V. J. Keast, *Mater. Charact.*, 2012, **73**, 1–7.

113 F. Hofer, F. P. Schmidt, W. Grogger and G. Kothleitner, *IOP Conf. Ser. Mater. Sci. Eng.*, 2016, **109**, 012007.

114 H. Tan, J. Verbeeck, A. Abakumov and G. Van Tendeloo, *Ultramicroscopy*, 2012, **116**, 24–33.

115 R. Brydson, *Electron Energy Loss Spectroscopy*, CRC Press, 1st edn., 2020.

116 P. Torruella, R. Arenal, F. De La Peña, Z. Saghi, L. Yedra, A. Eljarrat, L. López-Conesa, M. Estrader, A. López-Ortega, G. Salazar-Alvarez, J. Nogués, C. Ducati, P. A. Midgley, F. Peiró and S. Estradé, *Nano Lett.*, 2016, **16**, 5068–5073.

117 B. Goris, S. Turner, S. Bals and G. Van Tendeloo, *ACS Nano*, 2014, **8**, 10878–10884.

118 G. Möbus and B. J. Inkson, *Appl. Phys. Lett.*, 2001, **79**, 1369–1371.

119 M. Weyland and P. A. Midgley, in *Conference Series Institute of Physics*, Philadelphia; Institute of Physics; 1999, 2001, vol. 168, pp. 239–242.

120 S. M. Collins and P. A. Midgley, *Ultramicroscopy*, 2017, **180**, 133–141.

121 O. L. Krivanek, A. J. Gubbens, N. Dellby and C. E. Meyer, *Microsc. Microanal. Microstruct.*, 1992, **3**, 187–199.

122 L. Yedra, A. Eljarrat, R. Arenal, L. López-Conesa, E. Pellicer, A. López-Ortega, M. Estrader, J. Sort, M. D. Baró, S. Estradé and F. Peiró, *Analyst*, 2016, **141**, 4968–4972.

123 K. Jarausch, P. Thomas, D. N. Leonard, R. Twesten and C. R. Booth, *Ultramicroscopy*, 2009, **109**, 326–337.

124 B. Goris, M. Meledina, S. Turner, Z. Zhong, K. J. Batenburg and S. Bals, *Ultramicroscopy*, 2016, **171**, 55–62.

125 S. A. Theofanidis, V. V Galvita, C. Konstantopoulos, H. Poelman and G. B. Marin, *Materials*, 2018, **11**, 831.

126 S. D. Anderson, V. V Gwenin and C. D. Gwenin, *Nanoscale Res. Lett.*, 2019, **14**, 188.

127 S. Kim, J. M. Kim, J. E. Park and J. M. Nam, *Adv. Mater.*, 2018, 30, 1–24.

128 M. Estrader, A. López-Ortega, I. V. Golosovsky, S. Estradé, A. G. Roca, G. Salazar-Alvarez, L. López-Conesa, D. Tobia, E. Winkler, J. D. Ardisson, W. A. A. Macedo, A. Morphis, M. Vasilakaki, K. N. Trohidou, A. Gukasov, I. Mirebeau, O. L. Makarova, R. D. Zysler, F. Peiró, M. D. Baró, L. Bergström and J. Nogués, *Nanoscale*, 2015, **7**, 3002.

129 A. Feld, A. Weimer, A. Kornowski, N. Winckelmans, J.-P. Merkl, H. Kloust, R. Zierold, C. Schmidtke, T. Schotten, M. Riedner, S. Bals and H. Weller, Prof. Dr., *ACS Nano*, 2018, **13**, 1, 152-162.

130 Z. Saghi, D. J. Holland, R. Leary, A. Falqui, G. Bertoni, A. J. Sederman, L. F. Gladden and P. A. Midgley, *Nano Lett.*, 2011, **11**, 4666–4673.

131 R. Leary, P. A. Midgley and J. M. Thomas, *Acc. Chem. Res.*, 2012, **45**, 1782–1791.

132 C. J. Chen, R. K. Chiang, H. Y. Lai and C. R. Lin, *J. Phys. Chem. C*, 2010, **114**, 4258–4263.

133 J. Nelayah, M. Kociak, O. Stéphan, F. J. García de Abajo, M. Tencé, L. Henrard, D. Taverna, I. Pastoriza-Santos, L. M. Liz-Marzán and C. Colliex, *Nat. Phys.*, 2007, **3**, 348–353.

134 E. Ringe, B. Sharma, A. I. Henry, L. D. Marks and R. P. Van Duyne, *Phys. Chem. Chem. Phys.*, 2013, **15**, 4110.

135 G. C. Franks, C. Girard, A. Bruyant and A. Dereux, *J. Microsc.*, 2008, **229**, 302–306.

136 A. Losquin, L. F. Zagonel, V. Myroshnychenko, B. Rodríguez-González, M. Tencé, L. Scarabelli, J. Förstner, L. M. Liz-Marzán, F. J. García de Abajo, O. Stéphan and M. Kociak, *Nano Lett.*, 2015, **15**, 1229–1237.

137 A. Hörl, A. Trügler and U. Hohenester, *Phys. Rev. Lett.*, 2013, **111**, 1–5.

138 M. Kociak and O. Stéphan, *Chem. Soc. Rev.*, 2014, **43**, 3865–3883.

139   A. L. Koh, K. Bao, I. Khan, W. E. Smith, G. Kothleitner, P. Nordlander, S. A. Maier and D. W. McComb, *ACS Nano*, 2009, **3**, 3015–3022.

140   M. Mayer, L. Scarabelli, K. March, T. Altantzis, M. Tebbe, M. Kociak, S. Bals, F. J. García de Abajo, A. Fery and L. M. Liz-Marzán, *Nano Lett.*, 2015, **15**, 5427–5437.

141   B. Goris, G. Guzzinati, C. Fernández-López, J. Pérez-Juste, L. M. Liz-Marzán, A. Trügler, U. Hohenester, J. Verbeeck, S. Bals and G. Van Tendeloo, *J. Phys. Chem. C*, 2014, **118**, 15356–15362.

142   Y. Ding and Z. L. Wang, *J. Electron Microsc.*, 2005, **54**, 287–291.

143   O. Nicoletti, F. De La Peña, R. K. Leary, D. J. Holland, C. Ducati and P. A. Midgley, *Nature*, 2013, 80–84.

144   S. M. Collins, E. Ringe, M. Duchamp, Z. Saghi, R. E. Dunin-Borkowski and P. A. Midgley, *ACS Photonics*, 2015, **2**, 1628–1635.

145   A. Horl, G. Haberfehlner, A. Trugler, F. P. Schmidt, U. Hohenester and G. Kothleitner, *Nat. Commun.*, 2017, **8**, 1–6.

146   G. Haberfehlner, F. P. Schmidt, G. Schaffernak, A. Hörl, A. Trügler, A. Hohenau, F. Hofer, J. R. Krenn, U. Hohenester and G. Kothleitner, *Nano Lett.*, 2017, **17**, 6773–6777.

147   A. Skorikov, W. Heyvaert, W. Albecht, D. M. Pelt and S. Bals, *Nanoscale*, 2021, **13**, 12242–12249.

Short Bio:

Kellie Jenkinson is a postdoctoral fellow working with Professor Sara Bals at the Electron Microscopy for Materials Science (EMAT) research facility at the University of Antwerp (Belgium). She received her PhD under the supervision of Dr Andrew Wheatley at the University of Cambridge (UK, 2020) focussing on the synthesis and application of metal nanoparticles for plasmonics and electrocatalysis. During this time, she received a JSPS postgraduate research scholarship at Nogoya university (Japan, 2016) with the Noyori and Naka research groups. Her current research interests include in situ and operando electron microscopy characterization of nanomaterials under realistic environments in 3D.

Prof. Luis Liz-Marzán

Luis Liz-Marzán is Ikerbasque Professor at CIC biomaGUNE, in San Sebastián (Spain), where he also served as the Scientific Director from 2012 to 2021. PhD in chemistry from the University of Santiago de Compostela, he was postdoc at Utrecht University and Professor at the University of Vigo (1995–2012). He is a member of the Spanish Royal Academy of Sciences and Academia Europaea, among other awards and recognitions. Liz-Marzán has contributed to develop the colloidal synthesis and self-assembly of metal nanocrystals, as well as the characterization and application of their plasmonic properties. His most recent research focuses on the biomedical applications of plasmonic nanostructures.

Sara Bals is a full professor at the University of Antwerp (Belgium) and spokesperson of the Electron Microscopy for Materials Science (EMAT) research facility. She received her PhD from the same institution under the supervision of Professor Gustaaf Van Tendeloo. She did postdoctoral work at the National Center of Electron Microscopy in Berkeley, USA. Her expertise is in the combination of state-of-the-art electron microscopy with 3D reconstruction algorithms and the development of electron tomography for functional nanomaterials. 3D measurements of morphology and composition of nanomaterials are now also performed under realistic conditions to investigate the behaviour of nanomaterials during applications.